Scanning probe techniques as an investigation tool for semiconductor nanostructures and devices

Colvin, Jovana

2019

Document Version:
Publisher's PDF, also known as Version of record

Scanning probe techniques as an investigation tool for semiconductor nanostructures and devices

Jovana Colvin

LUND
UNIVERSITY

DOCTORAL THESIS
by due permission of the Faculty of Science, Lund University, Sweden
To be defended in the Rydberg Lecture Hall at the Department of Physics,
November 08, 2019, at 9:15.

Faculty opponent:
Prof. Edward T. Yu
The University of Texas at Austin

Organization	Document name
LUND UNIVERSITY Department of Physics Box 118 SE–221 00 LUND Sweden	**DOCTORAL DISSERTATION** Date of disputation 2019-10-08 Sponsoring organization
Author Jovana Colvin	

Title

Scanning probe techniques as an investigation tool for semiconductor nanostructures and devices

Abstract

Semiconductor nanostructure based devices provide new opportunities for contributing to a sustainable energy usage. This includes harvesting of energy (solar cells) and saving of energy, e.g. in lighting (light-emitting diodes, LEDs) and transfer of energy (power devices). However, development and improvement of nanostructure devices requires thorough characterization and understanding on a single nanostructure level. At nanometer dimensions, surface effects start dominating device performance. Therefore, macroscopic bulk characterization techniques are insufficient, and surface-sensitive tools are needed. Here, I used various types of scanning probe microscopy to investigate and manipulate surface and material properties of nanostructure devices that are relevant for energy saving and harvesting.

In(Ga)P nanowire diodes are promising candidates for photovoltaic applications. Kelvin probe microscopy (KPM) and scanning tunneling microscopy (STM) were used to investigate surface band alignment of a nanowire *p-n* junction. In addition, a novel method for optoelectronic characterization of individual nanowires without any processing steps is demonstrated. STM was utilized to both image and contact individual upright standing InGaP nanowires, obtaining current-voltage characteristics and solar cell figures of merits in dark and under illumination, for as-grown nanowires and after in-situ surface modification.

InGaN nanostructures are attractive for LEDs, because the luminescence of InGaN alloys could potentially cover the entire visible range by tuning the In content. The nanowire geometry allows combination of lattice mismatched materials. Nanowire-based InGaN platelet LEDs with varying In content as well as In quantum dots were studied by atomic force microscope (AFM), correlating surface corrugation with optical properties and investigating nucleation of surface facets.

GaN offers principally superior material properties for power electronic devices compared to the currently used Si and SiC, but a reduction of the defect density is required. We investigated low-defect GaN planar layers formed by reformation of GaN nanowire arrays. AFM, conductive-AFM, KPM, and scanning capacitance microscopy were utilized to investigate formation and distribution of different types of defects and their influence on GaN electrical properties. Furthermore, the revelation of defect-related conductive paths through AFM-induced anodic oxidation was explored.

Key words

III-V semiconductors, AFM, STM, KPM, SCM, c-AFM,crystal growth, doping, defects

Classification system and/or index terms (if any)

Supplementary bibliographical information		Language English
ISSN and key title		ISBN 1234567890 (print) 0987654321 (pdf)
Recipient's notes	Number of pages 213	Price
	Security classification	

Scanning probe techniques as an investigation tool for semiconductor nanostructures and devices

Jovana Colvin

LUND
UNIVERSITY

Faculty of Science, Department of Physics

ISBN: 978-91-7895-312-7 (print)
ISBN: 978-91-7895-313-4 (pdf)

Printed in Sweden by Media-Tryck, Lund University, Lund 2019

To my parents

"Crystals are like people, it is the defects in them which tend to make them interesting."

Colin Humphreys

Contents

List of publications

This thesis is based on the following publications, referred to by their Roman numerals:

I **Surface and dislocation investigation of planar GaN formed by crystal reformation of nanowire arrays**

J. Colvin, R. Ciechonski, F. Lenrick, O. Hultin, M. Khalilian, A. Mikkelsen, A. Gustafsson, L. Samuelson, R. Timm, B.J. Ohlsson

Phys. Rev. Materials 2019, 3, 093604

I planned and performed all scanning probe measurements and I selected and implemented the methodologies suitable to investigate the reported samples and tasks. I was involved in the TEM work, analyzed the data, and wrote most of the manuscript.

II **Local defect-enhanced anodic oxidation of reformed GaN nanowires**

J. Colvin, R. Ciechonski, A. Gustafsson, Lars Samuelson, B.J. Ohlsson, R. Timm

Submitted

I planned and performed all scanning probe measurements and I selected and implemented the methodologies suitable to investigate the reported samples and tasks, analyzed the data, and wrote most of the manuscript.

III **InGaN Platelets: Synthesis and Applications toward Green and Red Light-Emitting Diodes**

Z. Bi, F. Lenrick, **J. Colvin**, A. Gustafsson, O. Hultin, A. Nowzari, T. Lu, R. Wallenberg, R. Timm, A. Mikkelsen, B.J. Ohlsson, K. Storm, B. Monemar, L. Samuelson

Nano Lett. 2019, 19, 2832–2839

I performed AFM measurements and took a part in discussion and writing the manuscript.

IV **Growth of high quality InGaN platelets on a dome-like surface obtained by chemical mechanical polishing of InGaN pyramids**

Z. Bi, T. Lu, **J. Colvin**, E. Sjogren, N. Vainorius, A. Gustafsson, J. Johansson, R. Timm, F. Lenrick, M-E. Pistol, R. Wallenberg, B. Monemar, L. Samuelson

In manuscript

I performed AFM measurements and contributed to the discussion of the results and revision of the manuscript.

v **Self-assembled InN quantum dots on side facets of GaN nanowires**

Z. Bi, M. Ek, T. Stankevic, **J. Colvin**, M. Hjort, D. Lindgren, F. Lenrick, J. Johansson, L.R. Wallenberg, R. Timm, R. Fiedenhans'l, A. Mikkelsen, M.T. Borgstrom, A. Gustafsson, B.J. Ohlsson, B. Monemar, L. Samuelson

Journal of Applied Physics 2018, 123, 164302

II performed AFM measurements and took part in discussion and writing the manuscript.

vi **Operando surface characterization of an InP p-n junction nanowire diode**

S.R. McKibbin, **J. Colvin**, J.V. Knutsson, A. Troian, J. Webb, G. Otnes, K. Dirscherl, H. Sezen, M. Amati, L. Gredoriatti, M. Borgstrom, A. Mikkelsen, R. Timm

Submitted

I performed SPM measurements and took part in the XPS measurements and discussions about the manuscript.

vii **Photovoltaic Characterization of Individual In(Ga)P Nanowires Using a Scanning Tunneling Microscope**

J. Colvin, J. Brask, G. Otnes, M. Borgstrom, A. Mikkelsen, R. Timm

In manuscript

I planned and implemented the STM measurements. I took part in the XPS measurements, analyzed most of the data, and wrote part of the manuscript.

All papers are reproduced with permission of their respective publishers.

Publications not included in this thesis:

Low Trap Density in InAs/High-k Nanowire Gate Stacks with Optimized Growth and Doping Conditions

J. Wu, A.S. Babadi, D. Jacobsson, **J. Colvin**, S. Ynhman, R. Timm, E. Lind, E. Wernersson
Nano Lett. 2016, 16, 4, 2418-2425

Vertical cavities based on dislocation-free and atomically flat III-nitride hexagonal micro-prisms

M. Khalilian F. Hjort, Z. Bi, J. Johansson, F. Lenrick, O. Hultin, **J. Colvin** , M. Bengths, J. Bengtsson, J. Gustavsson, R. Timm, L. Wallenberg, J. Ohlsson, M-E Pistol, A. Haglund, A. Gustafsson, L. Samuelson
Submitted

Acknowledgments

Although many people participated in the practical and the theoretical creation of this thesis, it is necessary to express special appreciation and a great respect to some of my current and former colleagues for all that they showed and taught me during my doctorate.

Rainer Timm, thank you for opening the magical door of nanoscience and taking me through this research, for not allowing me to stop when I fall short, to quit when I get demoralized. Your striving strength and peaceful persistence led me to this station. In doing so, you let me have independence in experiments, you were not exclusive in giving tasks and opinions, which awakened my research spirit and gave me enthusiasm for work. The entire time you were my teacher, colleague, support, the foundation of my experiments, the coordinator of all my work until the end of my PhD. Thank you!

Anders Mikkelsen, thank you for being there when I needed you, following my work inconspicuously and giving me the freedom to think, but guided me through ideas.

Jonas Ohlsson, together we walk the world of nitrides; you taught me the art of GaN epitaxy, and in doing so, enchanted me with it. This was, of course, followed by an immense amount of involvement, for which you've sacrificed your time and work. And that is invaluable to me, thank you!

Chris Palmstrøm, you accepted me to your research group and as a token of maximum welcome allowed me to dismantle your favorite cryo-SFM. Is there a more genuine hospitality and faith in the newcomer? Thank you. Thanks to Mihir Pendharkar, Dan Pennachio, Nate Wilson, and Tobias Brown for a wonderful time and support in the Palmstrøm's lab. Mihir Pendharkar, you made me understand that the science is not a benefit of an individual, but a product of the exchange of opinions, freedom of information, and the filtrate of many experiences of the people involved in it. Thank you.

Nitride community, my second home, thank you for your warm hospitality and inspirational Tuesday's meetings. Lars Samuelson, thank you for welcoming me to your group and giving me the opportunity to collaborate with the fantastic minds in it. Rafal Ciechonski, you helped me immensely by growing the samples I worked on, thus allowing me better characterization. Our combined effort resulted in improved reformation (and will result in even better). Zhaoxia Bi, thank you for all the knowledge and joy you have given me. I will always remember the inward joy while contacting a single nanoplatelet with the STM and seeing it shine blue. You brought this sample to me. With you I share most papers although, making you begin writing them seemed to take centuries. Luckily, time is a relative category, and I am not necessary a role model. You have shown your speed of efficiency and ability on the last manuscript which gave me a chance to include it in this work. Thank you. Anders Gustafsson, thank you for all the CL measurements, curiosity, insights, and

help you have provided. Taiping Lu and Olof Hultin, thank you for kindly sharing your knowledge.

In(Ga)P community, and my former colleagues Xulu Zeng, Alexander Berg, Gaute Otnes, thanks for their great collaboration and epitaxial work on the samples that I started my work on. My later commitment to nitrides did not throw you into oblivion, only my curiosity happen to take me in another direction.

Filip Lenrick, thank you for always finding the time for my experiments, heartily explaining every move along the way. Also, thanks to you, I know how to make lamellas.

Synchrotron research, the group I officially belong, thank you for your wholehearted support in bringing my commitment and interest in nanostructures to its finish. Olof Persson, you have taken the time to teach me to work on the STM, it meant a lot to me. Sophie Yngman, you have successfully attracted me into the world of AFM when you presented its characteristics in a very impressive manner during our class. Bravo and thank you for this. Oliver Scholder, thank you for discussions and fun times with the Rubik's cube. It activated my brain folds for variability of ideas. Ren Zhe, in trying to combine AFM with x-rays, you crowned every potential failure with success. You have taught me to be a team player. Thanks for the wonderful collaboration.

Erik Malm, you deserve a special thanks for the flights in the air and the steps on the ground. You were always there for everything I needed, for work incentives, for advises, and assistance. Thanks to you, I was able to rise and reach my goal!

Thank you all!

Popular science summary

Semiconductor crystal structures and devices of nanometer (10^{-9}m) dimensions are usually called nanostructures. They can take variety of shapes (viz. rod-like wires, pyramids, platelets). Their small dimensions allow efficient use of material and a tolerance for combining different material combinations while retaining high crystal fidelity. They may also function as efficient crystal dislocation filter, capable of significantly reducing their prevalence, when growing on parent substrates with high dislocation density. As such, semiconductor nanostructures provides alternative paths towards improvements in semiconductor device-technologies such as light emitting diodes, solar cells, and power electronics.

But alternative paths require alternative means for acquiring knowledge, in this case understanding of characteristics and performance of individual nanostructures. At this scale, many of the bread and butter techniques for characterization of conventional, planar, semiconductors fail, often by missing dimensional information or being statistical in nature, averaging over larger areas or volumes. This is where scanning probe microscopy (SPM) technologies steps in. SPM comprises a broad family of, most often, nondestructive surface-sensitive techniques, utilizing a sharp tip being scanned over a surface as local probe. Different SPM techniques use different tip-surface interactions, well known examples being scanning tunneling microscopy (STM) and atomic force microscope (AFM). STM is based on electron tunneling between the tip and the surface, the tunneling current providing feedback-information while in AFM interaction forces provide feedback information as the tips scan the surface. AFM is often modified to provide complementary information. Besides topography, AFM is capable of simultaneously measuring local current (conductive-AFM), surface potential difference (Kelvin probe microscopy), and doping in semiconductors (scanning capacitance microscopy). Accordingly, AFM allows probing of mechanical, structural, and electrical, properties of materials at the nanoscale. Being an interactive characterization technology, SPM can also be used for modification and manipulation on the nanoscale. The utilization of such techniques has enabled additional understanding of some of the nanostructures investigated in this work.

Nitride semiconductors, and especially GaN (gallium nitride) offers superior electronic properties for applications requiring high power or high speed/medium power. Within these applications, it would be a much more energy efficient material than silicon, the semiconductor material with historical dominance in the electronics industry. However, an obstacle for widespread adoption of GaN is the lack of a high quality GaN wafers. GaN grown on dissimilar materials leads to high amounts of dislocations, leading to leakage and failures in power-electronic devices. In this study, a novel approach to form planar GaN films, by growth and reformation of nanowires, was investigated. This research may potentially improve power electronic substrates. A combination of complementary SPM studies resulted in an in-depth understanding of the distribution, origin and formation

of defects in these layers, providing critical understanding for further development of this approach.

The InGaN nanostructured LEDs investigated in this thesis are grown from nanowire-based platelet geometry. One beautiful aspect of the InGaN semiconductor alloy is that it, when used for LEDs, can cover the entire visible spectrum, by tuning the In/Ga ratio. And actually some more, going from infrared (InN) to ultraviolet (GaN). However, by increasing the In content in InGaN grown on GaN substrate, the lattice mismatch between the crystals also increases, causing strain which typically results in defects and cracks. In this work, AFM was used to study InGaN platelets at different stages of evolution, confirming crystal fidelity and flatness on atomic level.

Solar cells are used to harness renewable energy from the sun. InGaP is a promising solar cell material due to its capacity to transform a large portion of the solar light into energy. A clean, novel, and relatively quick method of examining photovoltaic behavior of an individual InGaP nanowire diode junction was established using STM. The STM operates in ultra-high vacuum, offering the possibility to examine the surface properties and processing steps required for improving device performance. The STM tip is used to both image and investigate current-voltage (*I-V*) properties in dark and light on upright-standing NWs. Kelvin probe microscopy was also used for studying InGaP nanowire diode junctions.

Chapter 1

Introduction

1.1 Motivation

To tamper global warming it has become clear that we need to move towards higher levels of sustainability by transforming our entire infrastructure. Semiconductor nanostructures based devices provide new opportunities for contributing to a sustainable energy usage. This include harvesting of energy (solar cells) and saving of energy e.g. in lighting (LEDs) and transfer of energy (power devices). This thesis touches on all three fields, which the following paragraphs provide general introduction to. After this, I discuss how III-V nanostructures may provide paths to improvements, and how characterization by scanning probe microscopy contributes.

Sustainable energy sources rely on harnessing renewable energy from hydro power, wind, and solar. In 2018, renewables generated 32.3 % of Europe's electricity which accounts to a rise of 12 % from 2010 [1]. Photovoltaics is the fastest increasing renewable energy source and it is already competing favorably in cost to fossil fuels. Between 2017 and 2018 the number of grid connected solar PV systems in Sweden increased by 67 %. To date, silicon is the most commonly used material for solar cell fabrication accounting to approximately 90 % of installed modules. However, silicon based solar cells are close to reaching their theoretical limit at around 25 %, and require very large footprint on the land in terms of materials and size. Most promising alternatives are direct band gap materials consisting of group III and V elements. An excellent candidate is InP due to its narrow and direct band gap (1.34 eV) capable of absorbing a large portion of the solar spectrum. However, III-V bulk materials would drive the prices up to the point where solar cells would not even be considered.

Light emitting diodes (LEDs) are substantially reducing the energy consumption as sub-

stitutes for incandescent light sources. In the United States alone, the LED is estimated to save 348 TWh by the year 2027, compared to no LED use. To put this into perspective, 348 TWh is equivalent to the annual electrical output of 44 power plants, each 1000 MW [2]. This is attributed to the low energy consumption of LEDs and the prices being driven down to the point where it is not anymore a primary cost component of the integrated lighting product. The white LED revolution was enabled by the development of the blue InGaN/GaN LED, which can reach up to 90 % efficiency. White light is primarily achieved by down-conversion of the blue light with a phosphor, most often adding a broad yellow peak. Although more efficient than the white light produced by its predecessors (incandescent and fluorescent tube lamps), the white LED loses about 25% of its energy in the phosphor down-conversion process to longer wavelengths. Still, other color LEDs (green, yellow, and red) remain at lower efficiency. One of the potential paths for providing pure RGB LED combinations is the development of efficient red and green InGaN LED. InGaN is a direct band gap material with a luminescence wavelength that can possibly cover the entire visible range by varying the In/Ga ratio. However, achieving sufficient In content for reaching green and red luminescence is challenging.

Regardless of the primary source of energy (renewable or not), elimination of power losses during power conversion requires special attention. Today's silicon power devices are inefficient due to the material limits of silicon. The GaN semiconductor material is a better alternative due to its excellent properties, characterized by high band gap, high electron mobility, and high thermal stability. A transition to GaN-based power electronics can theoretically allow elimination of 90 % of losses associated with power conversion. In addition, higher thermal conductivity of GaN as compared to Si allows devices that are physically smaller. This is of importance because the space real-estate is becoming more expensive. However, before we can fully utilize the potential of GaN, development of large scale substrate with improved material quality is needed. Commercial GaN is grown on dissimilar materials leading to high dislocation densities, resulting in leakage and premature device failure.

Nanostructures investigated in this dissertation are anisotropic monolithic crystals that are available in different flavors of shape, size, crystal phase, orientation, and composition, enabling improvement of existing applications in electronic and optoelectronic devices, but also leading to novel applications in a wide range of fields. When talking about nanostructures it is often that we refer to nanowires (NW, long and narrow crystals) and nanoplatelets (thin and wide). Nanostructures are typically synthesized either by a bottom-up approach, where individual atoms via chemical bonding build up nanostructures of interest. Another method is a top-down approach where nanostructures are fabricated by means of size reduction of larger structures. It is also possible to combine the two methods via hybrid approach. One of the representative techniques utilized for the growth of III-V semiconductor nanostructures is metal-organic vapor phase epitaxy (MOVPE). In this dissertation

the III-V nanostructures are grown with MOVPE, they are mainly NW based, and all synthesized by bottom up approach.

Group III-V alloys are a wonderful material system that allows a wide range of structures and devices to be made by redesigning their properties through a combination of different materials (heterostructures), band gap tuning, etc. However, in conventional devices the heterostructure has to be carefully lattice matched to not introduce defects. Furthermore, the source material for III-V growth is very expensive compared to Si wafer growth, and some of the elements are increasingly rare. The III-nitride subgroup is also haunted by the insufficient bad crystal quality due to the lack of native substrates. Nanowires and other nanostructures offer structural advantages to conventional planar geometry, many related to their small footprint, allowing elastic relaxation of the crystal lattice. With their excellent inherent properties of strain relaxation around their periphery, NW allow epitaxial stacking of materials varying in lattice parameter and band gap, enabling novel heterostrucure design. Epitaxial growth of a heterojunction within a single nanowire offers a potential avenue for highly efficient multi junction solar cells. Longer wavelength InGaN LEDs can be explored by tailoring the Ga/In ratio, where the small footprint of NWs allows them to act as an excellent dislocation filter, significantly reducing the dislocation density when grown on high dislocation density substrates. This means that also we have the ability to potentially grow high quality GaN films formed from coalesced NWs for power conversion applications. The high cost of III-V semiconductors becomes the problem for massive use as in solar cells. The nanostructure dimensions allow less consumption of expensive material. In addition, NW geometry with their high aspect ratio that enables reduced optical reflection and enhanced absorption [3].

In order to understand and improve NW based devices, a thorough characterization at the single nanostructure level is required. Unfortunately at this scale many generic semiconductor characterization methods are statistical and not well suited for nanostructures. Moreover, large scale contacts result in averaging over multiple nanostructures, in the worst case only showing the extreme points (best or worst). Even when contacting a single nanostructure, it is hard to avoid coverage of multiple facets with inherently different properties, again, averaging and leading to an incomplete understanding. A nondestructive thorough characterization revealing precise variations and features of individual nanostructures, such as the influence of individual structural defects, is vital as it provides the understanding required for improvement. This is where scanning probe techniques come to rescue!

Scanning probe microscopy (SPM) has become an indispensable tool for characterization on the nanoscale, providing means to visualize, examine, and modify properties of nanostructures, as shown through this dissertation. Atomic force microscopy (AFM) allows mapping of true topography and the ability to aim the probe within nm accuracy on the sample, and this gives its derivatives unique opportunities to utilize the tip as a special measurement instrument for a variety of properties. AFM based approaches for electrical

characterization, such as conductive AFM (c-AFM), Kelvin probe microscopy (KPM), and scanning capacitance microscopy (SCM), were used in this work for studying conductivity, surface potential and doping profiles of semiconductor nanostructures. c-AFM measurements provided insights into both the nature and electrical influence of individual defects in GaN NWs and coalesced films, resulting in improvements of growth and understanding of defect formation and distribution. KPM was used for studying In(Ga)P NW *p-n* junctions. Finally, a clean, novel, and relatively quick method of examining photovoltaic behavior of individual In(Ga)P *p-n* junction NWs was established using scanning tunneling microscopy (STM), offering the possibility to examine the surface properties and processing steps required for improving device performance.

1.2 Outline of the thesis

The work is divided into two parts: in part one, focus is placed on the topics required for understanding the papers presented in part two. Part I is divided into this introduction and three chapters:
Chapter 2 gives a general introduction to the material properties and epitaxy of III-V semiconductor nanostructures used in this thesis, specifically (In)GaN and In(Ga)P. It highlights the basic crystal properties, viz. crystalline structures, polarization, and defects. Then, I discuss the epitaxy and challenges of a verity of nanostructures (viz. platelets, nanowires, quantum dots) based on the above-mentioned materials.
Chapter 3 provides a background needed for understanding InGaP nanowire based solar cells and InGaN NW based LEDs. I also address the difficulties in the formation of these nanostructures.
Chapter 4 highlights different characterization techniques utilized during this thesis, each technique is introduced and the main parts of the results as they appear in the papers are highlighted.

Chapter 2

III-V semiconductors and their nanostructures

Semiconductors are a group of materials, usually crystals, with a number of properties that make them made them the main building blocks for electronic and optoelectronic devices. The most important property is that, though pure semiconductors are insulating, they can be tailored to conduct by negative charge carriers (electrons) or positive charge carriers (holes). This is related to another special property of semiconductors, the band gap, an energy regime without electronic states, separating valence band electronic states from the conduction band electronic states. The band gap allows a photon to excite an electron from the valence band to the conduction band creating an electron-hole pair. In a similar manner, the semiconductor may emit a photon by radiative recombination of electron-hole pair. To be a good light emitter, the dominating recombination process should be a direct process. In some semiconductors this is an indirect process, requiring an additional interaction with a phonon (crystal vibration). The elemental semiconductors Si and Ge are both indirect semiconductors, while most of the compound III-V semiconductors, which this thesis focus on, have direct band gaps.

In order to be able to discuss the work of this thesis, and the challenges it has addressed, a brief discussion about the crystal structure and its correlation with semiconductor properties will be given. I will discuss influence of defects in the crystal. This is followed by a brief discussion of epitaxy, the art of crystal growth and, specifically, growth of nanostructures.

2.1 Crystal structure and basic material properties

Most semiconductors tend to crystallize in a cubic fcc-based lattice. For the elemental semiconductors Si and Ge this is the diamond crystal structure, while most III-V semiconductors form a zincblende (ZB) lattice, as shown in Fig. 2.1(a). The ZB structure comprises two types of atoms, as exemplified by the group III element In and the group V element P, but it is otherwise similar to the diamond structure of the group IV elements. In fact, if we replace In and P in Fig. 2.1(a) with Si atoms we have the diamond structure.

While most III-V materials have strong energetic preference to crystallize in the ZB lattice, some of them preferentially form the wurtzite (WZ), hexagonal close-packed, structure. Group III-nitrides typically crystallize in a stable WZ lattice, as shown in Fig. 2.1(b). While only one lattice constant, a, is sufficient to represent the dimensions of the ZB crystal, the WZ unit cell requires two lattice constants, edge length $a = 3.189$ Å and prism height $c = 5.185$ Å, as shown in Fig. 2.1(a).

As highlighted in the left lower corner of (a) and by the shaded pyramids in (b), each atom is bound to four other atoms in a tetrahedral configuration. It is easy to see that the four bonds of a Si tetrahedron occupy the four valence electrons, such that the Si crystal satisfies the desired state of a full shell and no free bonds. The situation is similar for the InP, as the group III element In, with three valence electrons, together with the group V element P share a total of eight valence electrons, also fulfilling the full shell condition but with one of the V- electrons displaced to the group III element.

The symmetrical properties of the crystal provide a periodic electric field resulting in electronic energy levels common for the whole crystal, which means that charge-carriers can move between identical states in the crystal without losing kinetic energy. This and the interaction between many neighboring atoms, creating additional states in a quasi-continuous energy distribution, is translated to the concept of energy bands and a band gap, a regime of electronic kinetic energy without any electronic levels.

The insulating property of a textbook example (ideally pure) semiconductor derives from the fact that all valence band states are occupied by electrons, with no room for electron movement, while all states above the band gap, in the conduction band, are empty, with no electrons to work as charge carriers. That said, this ideal situation is only true for a perfect semiconductor crystal.

As mentioned, the band gap properties are determined by the periodic potential landscape of the semiconductor crystal. The differences are visualized in Table 2.1 where GaN and InN parameters are shown. This provides us with the option of band gap engineering using different III-V semiconductors. Beside binary alloys, such as GaN or InP, also ternary alloys, e.g. InGaN and GaInP, or more complex combinations can be realized. This opens up many

possibilities for tailoring material properties such as the band gap or the lattice constant, and to realize high-quality heterostructures (combinations of two or more dissimilar materials) through epitaxial growth, where e.g. the lattice constant is adjusted between both materials, but the band gap differs significantly. For example, exchanging 52 % of the In atoms in InP with Ga decreases the lattice constant, closely matching it to that of GaAs. Hence it is possible to grow $Ga_{0.52}In_{0.48}P$ with a relatively lattice match to GaAs.

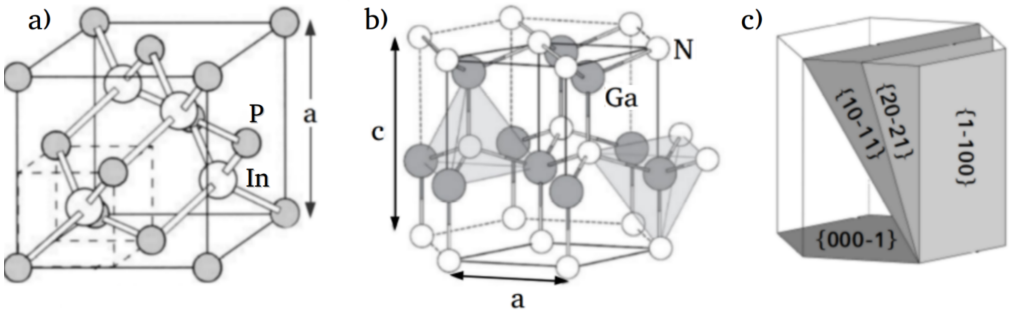

Figure 2.1: Crystal structure of (a) zincblende (b,c) wurtzite polytypes with three-dimensional view (a,b) and projection on the different lattice planes (c), adapted from [4].

Table 2.1: Lattice parameters (a,c), the internal displacement parameter (u), and band gap of two wurtzite III-N binary compounds, [4].

Parameters	**GaN**	**InN**
a (Å)	3.189	3.545
c (Å)	5.185	5.703
u^2	$0.376c$	$0.382c$
E_g (eV)	3.39	0.65
type	direct	direct

The additional anisotropy of the WZ crystal structure leads to very unique and interesting properties. Table 2.1 depicts the internal displacement parameter u, arising from this anisotropy, defined as group III-nitride bond length along the c direction, in the unit of c [4]. Polarity, arising from the noncentrosymmetry along the c-axis is defined by the direction of the III-N bonds in c direction, where $\langle 0001 \rangle$ +c direction is termed Ga-polar whilst $\langle 000\bar{1} \rangle$ -c direction is N-polar. Owing to a higher electronegativity of N compared to Ga, a negative surface fixed polarization charge results for the Ga-polar surface, and the positive for the N-polar surface, see Fig. 2.2. As a consequence a large electric field develops called spontaneous polarization (P_{SP}), illustrated in Fig. 2.2(a). Note, P_{SP} is canceled within the material, but at the cut of Ga and N- face there is an asymmetry that leads to spontaneous polarization. Spontaneous polarization occurs in an unstrained wurtzite crystal in -c direction.

In addition to polar c-planes (those with Miller indices $h = k = 0$), α-phase lattice planes can be non-polar ($l = 0$) or semi-polar (all other non-c planes with non zero l) [5]. On non-polar planes the net sum of charges at the surface is zero, while semi-polar planes result in an average spontaneous polarization close to zero.

In strained GaN, piezoelectric polarization (P_{PE}) occurs because of the electric field created by an offset of the ionic charges [4], illustrated in Fig. 2.2(b). This strain can be caused by the epitaxial growth of lattice mismatched materials. Deformation of the crystal due to growth onto a material with larger (smaller) lattice parameters induces tensile (compressive) stress and the angle θ_1 becomes wider (narrower). The polarity would of course be determined based on the type of stress (compressive or tensile). The undesirable effects of spontaneous and piezoelectric polarization on optoelectronic properties of InGaN are addressed in chapter 3 of this dissertation.

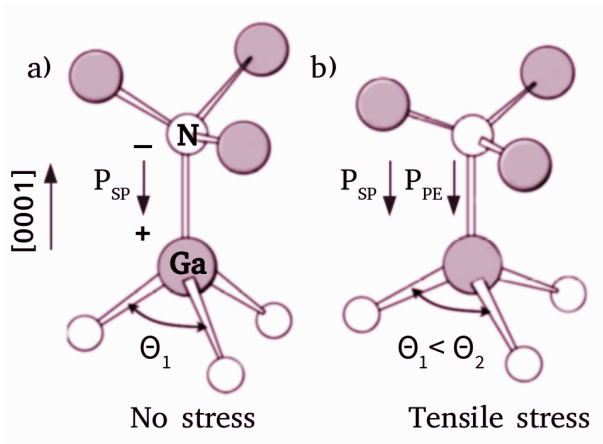

Figure 2.2: (a) Distribution of negative (positive) surface fixed polarization charges on Ga- (N-) polar facet due to the build in spontaneous polarization. (b) Piezoelectric polarization of ionic bonds in tetrahedron shape, modified from [6].

2.2 Defects in semiconductors

No crystal is perfect. The crystal lattice is bound to have imperfections. Some imperfections are intentionally introduced in semiconductors, allowing us to tune their electrical conductivity. After all, these characteristics are the ones that make semiconductors useful, providing the means for fabrication of electronic and optoelectronic devices, such as LEDs and solar cells, discussed in chapter 3. Defects can also have adverse effects on device performance and it is important to understand their origin and characteristics. This section briefly introduces the subject of crystal defects in semiconductors. Defects are most often incorporated during crystal growth but can also result from certain processing steps during device fabrication or, even, device operation. The following discussion attempts to relate

the crystal defects to their effect on electrical and optical properties, mainly in perspective of the energy states they may introduce in the band gap. First, point defects are discussed, followed by line defects, and finally area defects. Although other defects exist, such as stacking faults, free surfaces, twins, etc., these defects are beyond the focus of this thesis and will as such be omitted.

2.2.1 Point defects

Point defects are singular, atomic, irregularities in the periodicity of the crystal lattice. We distinguish between two groups of point defects: 1) atomic impurities from elements foreign to the crystal which are called extrinsic defects. 2) Atomic irregularities inferred by the native elements of the crystal matrix are called native or intrinsic defects. A common example of extrinsic defects is Si impurities in a GaN crystal. The Si atom may be situated at a Ga or N site and then denoted Si^{Ga} or Si^{N}, or it may be an interstitial impurity (in between the lattice sites). Similarly, native atoms can occupy a wrong lattice site forming native defects, such as N^{Ga} or Ga^{N} in GaN, as well as interstitial defects. Vacancies in the lattice, such as V^{N} or V^{Ga} also belong to the group of native defects.

Regardless of their type, point defects will influence the structure of the matrix lattice leading to a local perturbation of the energy bands. Depending on the chemical difference between the point defects and matrix atoms, defects may introduce allowed energy-levels within the forbidden band gap, where based on the position, they may be located close to a band edge (shallow-level defects) or deep within the band gap (deep-level defects).

Extrinsic point defects

Precisely controlling incorporation of impurities into the crystal structure is a process known as doping. This is done in order to control the conductivity of the semiconductor. Those impurities responsible for donating electrons to the conduction band are called donors. They form electron levels inside the band gap, close to the conduction band edge, and are called shallow if the electron can be promoted to the conduction band by thermal excitation at room temperature. Shallow levels are therefore responsible for doping. Impurities which form shallow levels close to the valence band edge with deficit electrons that can be filled by an electron from the valence band are called acceptors. In this sense, dopant impurities are characterized by their activation energy - that is the energy required to excite an electron (hole) from the donor (acceptor) impurity into the conduction (valence) band. A donor impurity exists in two charge states, neutral if the electron is bound to the impurity and positive when the electron is ionized to the conduction band. The acceptor impurity is negatively charged when the hole is free (filled bond), or it can be neutral when the acceptor has a hole bound to it (empty bond).

At low temperature, in an *n*-doped semiconductor, even most shallow donors are neutral, and the Fermi level is between the donor level and the conduction band edge to ensure charge neutrality. At room temperature, most donors are activated, the semiconductor is *n*-type, and the Fermi energy lies below the donor level. At very high temperatures, excitation of intrinsic charge carriers across the band gap becomes dominant, and the Fermi level moves toward the middle of the band gap, as shown in Fig. 2.3. Corresponding behavior is observed for the acceptors. If the impurity provides shallow acceptor levels, trapping electrons from the valence band, conduction will mainly occur in the valence band, through drift of positively charged holes (caused by the missing electrons in the valence band) and we conveniently refer to the impurity as a *p*-type dopant and the semiconductor as a *p*-type semiconductor. This situation with two types of charge-carriers, with opposite charge, allows formation of *p-n* junctions and with this a major part of semiconductor devices, as will be described in chapter 3.

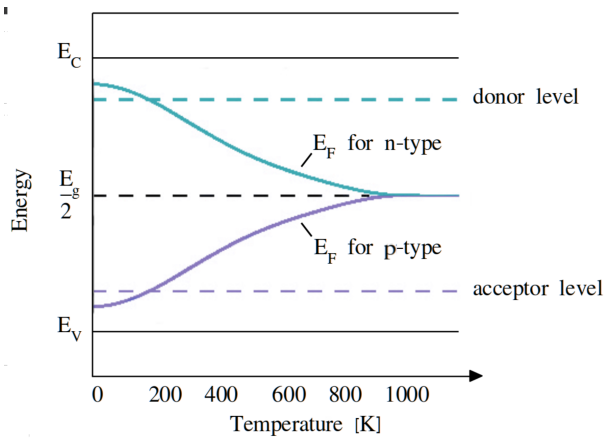

Figure 2.3: (a) Schematics of an *n*- and *p*-type semiconductor as a function of temperature.

At this point it is worth mentioning that some impurities introduce energy levels located far from the band edges, called deep-level impurities (DX or AX centers), responsible for charge trapping and/or nonradiative recombination centers [4]. A DX (AX) center occurs when an impurity that is expected to act as a donor (acceptor) instead undergoes a large lattice relaxation to trap an electron (hole) to become a deep acceptor (donor) [7]. These localized defect levels can act as traps for free carriers, harming the electrical and optical properties altering device performance.

Intrinsic point defects

The number of vacancies or native interstitials (n) are associated with the change in Helmholtz free energy ΔF:

$$\Delta F = nE_{\mathrm{f}} - T\Delta S \tag{2.1}$$

where E_{f} a defect formation energy (an important quantity: low E_{f} implies a high probability of defect incorporation, whereas defects with high E_{f} are not likely to form) and ΔS is the change in the entropy of the crystal, and T is the temperature [8]. In equilibrium, the concentration of defects is given by the ratio c_{o} of total number of defects by the total number of atomic sites as is approximately:

$$c_{\mathrm{o}} = \exp -\frac{E_{\mathrm{f}}}{k_{\mathrm{B}}T} \tag{2.2}$$

where k_{B} is Boltzmann's constant and T is the temperature in K. Typically interstitial have higher formation energy compared to vacancy [8].

Besides abovementioned defects, compound semiconductors may also incorporate antisite defects with a Ga atom, for instance, occupying a nitrogen site ($\mathrm{Ga^N}$), and vice versa.

Just like impurities, native defects introduce energy levels within the band gap and can be ionized, acting either as donors or acceptor. Moreover, native defects may interact with impurities (forming centers called complexes) and dislocations, resulting in electrical compensation or non-radiative recombination centers [9].

Point defects in GaN

Residual impurities such as oxygen [10, 11, 12, 13] and carbon have prominent effect on the conductivity of unintentionally doped GaN. Oxygen is, for example, known for high concentrations [14] (10^{16} cm^{-3} and above) in unintentionally doped GaN where it act as a shallow donor on N sites. The high concentration of oxygen found in GaN is what makes it one of the candidates for the high n-type background doping often observed in GaN. In addition to oxygen, gallium-site Si is an effective donor dopant [15] for purposely n-doping. Carbon is expected to be most stable on N ($\mathrm{C^N}$) sites acting as a deep level acceptor (contrarily to previous reports) having an ionization energy of 0.9 eV above the valence band [16]. The high ionization energy will prevent the rise of p-type conductivity, but will instead lead to the Fermi-level pinning near $\mathrm{C^N}$ transition level leading to semi-insulating GaN [17, 18]. Moreover, Lyons *et.al.* have shown that $C^{\mathbf{N}}$ gives rise to widely observed yellow luminescence (YL) in GaN [16, 19, 20].

In Paper I we show that the growth of unintentionally doped GaN NWs shows a signature of yellow band luminescence centered at 2.2 eV and increased background concentration

of electrons. In Paper II we investigate this further and a relationship is established between point defects and the observed *n*-type conductivity of NW cores.

2.2.2 Dislocations

Dislocations are defined as a change in the atomic periodicity of a crystal along a dislocation line. An important parameter used to classify the nature of a dislocation is the Burgers vector given by a Burgers circuit. Assuming a crystal containing a dislocation, a Burgers circuit would be an atom-to-atom path around the dislocation forming a closed loop, as shown in Fig. 2.4. Following the same path, the circuit would fail to close in the perfect crystal structure. The vector required to complete the Burgers circuit is denoted as Burgers vector, denoted QM in Fig. 2.4(b), which gives the unit slip distance, or crystal lattice shift, in terms of magnitude and direction [8].

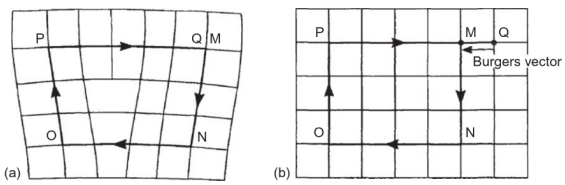

Figure 2.4: Burgers circuit (a) around dislocation and (b) in the perfect crystal. The Burgers circuit from the dislocation fails to close in a perfect crystal, from [8].

Dislocations can then be classified as: 1) edge-type, if their crystal lattice shift, **b**, is normal to the dislocation line, 2) screw-type, if **b** is parallel to the dislocation line, and 3) mixed if **b** is neither normal nor parallel to the dislocation line, but a combination of edge and screw.

Figure 2.5 shows a schematic of an edge (bottom) and screw (top) dislocation in a simple cubic crystal arising when the crystal lattice shifts. For an edge dislocation an extra plane of atoms is inserted into the crystal resulting in compressive stress in the part of the crystal where the plane is inserted, and likewise tensile stress in the opposite. The dislocation line is perpendicular to **b**. However, the dislocation line may be parallel to **b** when the planes are displaced from each other through a shear, as is the case with a screw dislocation. In order for the screw dislocation to traverse through the crystal, the action of gliding is required, with an effort much larger than that of moving a dislocation along a single plane.

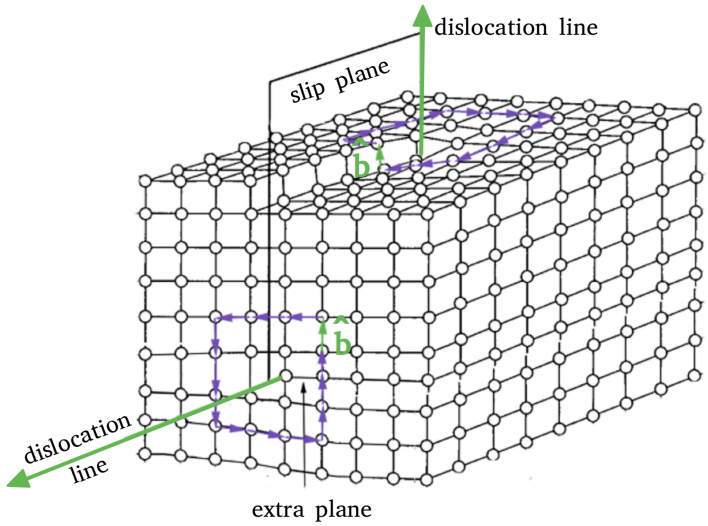

Figure 2.5: Schematics of an edge (bottom) and screw (top) dislocation in a simple cubic crystal.

Threading dislocations in GaN

GaN and other III-N materials lack an affordable and scalable way of creating bulk wafers. They ares usually grown heteroepitaxially (growth of different crystals on each other) on other commercially available substrate materials. Most common are Si and SiC substrate for electronic applications and α-phase sapphire (Al_2O_3) for LED fabrication. The difference in the a lattice constant of GaN (3.189 Å) and sapphire (4.785 Å) results in a lattice mismatch of 15.04 % (in the basal plane), taking into an account a 30° rotation of sapphire relative to wurtzite GaN. To accommodate the larger sapphire lattice constant, tensile strain fields develop in the GaN film during growth, which typically is done at temperatures of 1000° C and above. Upon cooling down to room temperature a compressive strain will develop in GaN due to a smaller thermal expansion coefficient relative to sapphire. This combination of lattice and thermal mismatch is the origin of dislocations, termed threading dislocations (TDs) (edge, screw, or mixed dislocations), formed by GaN growth on foreign substrates. Their mechanism of origin is highlighted by associated Burgers vectors: edge dislocations are formed in [0001] direction with $\mathbf{b} = 1/3\ \{11\bar{2}\bar{0}\}$, and screw dislocations with $\mathbf{b} = [0001]$ [21, 22].

The strain field around a dislocation can getter point defects, which move by diffusion in the crystal (viz. Ga vacancies, oxygen and their complexes). Because dislocations can be decorated by different defects, they will ultimately have different electrical nature, depending on the prevalence of point defects in the crystal. The effect of a dislocation will depend on its core's nature (type of dislocation), and the charge of dislocation core.

Strain around dislocations can be visualized by transmission electron microscope. Furthermore, cathodoluminescence is good for imaging non-radiative recombination centers originating from dislocations. Interestingly, the type of threading dislocation can be identified by their surface termination, using atomic force microscope [23]. Figure 2.6 shows an AFM image of a GaN surface. Pure screw and those of mixed character terminate at least one surface step, as seen in 2.6(a) and 2.6(c), whereas pure edge TDs terminate on the terrace, seen in 2.6(b).

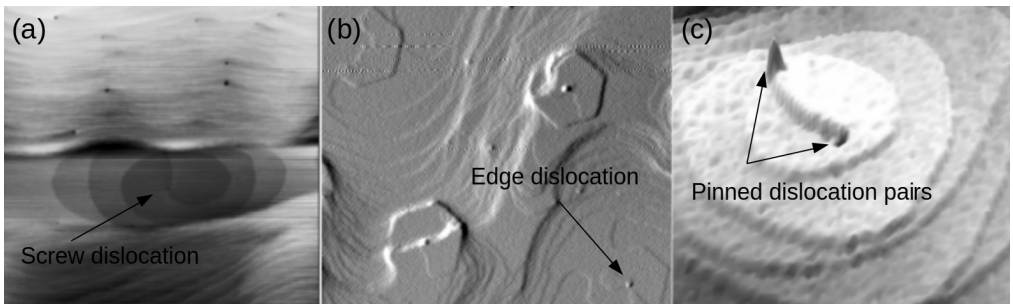

Figure 2.6: AFM image of GaN surface highlighting (a) screw, (b) edge, and (c) pinned dislocations.

2.2.3 Inversion domains

Here the focus is placed on an extended type of defect in polar materials: inversion domain (ID). An ID is a crystal section of opposite polarity to the one of the primary crystal matrix. IDs are known to nucleate at substrates which lack the polar symmetry, such as sapphire, but can also form due to the appearance of aluminum or magnesium or different growth conditions (e.g., growth technique, substrate pre-treatment). An important consequence in dual polarity systems is the resulting opposing piezoelectric field whose effect on nanostructure based devices is still unknown.

A quick and straightforward method of determining the polarity of a GaN crystal is selective etching in a hydroxyl solution at a slightly elevated temperature, most commonly used etchants being KOH or NaOH. As discussed in the previous section, each atom binds to the crystal in a tetrahedral configuration of four bonds. The terminating atom on the polar $\{0001\}$ planes binds to three underlying atoms in the crystal but the charge of the dangling bonds will be different for the Ga-terminated (0001) group-III cation surface and the N-terminated $(000\bar{1})$ group V anion surface. On the N-terminated surface, hydroxyl reacts with a single dangling positive bond on Ga to form Ga and OH complexes [24]. When all of the dangling bonds are saturated, on a $(000\bar{1})$ surface, OH^- ions can be chemically adsorbed onto the back-bond of Ga, see Fig. 2.7 step (2), forming gallium oxide (Ga_xO_y) and NH_3 (2-3). Furthermore, gallium oxide is dissolved in hydroxyl solution that acts as a catalyst (4), so that the first bilayer is completely removed. Continuation of etching

will essentially dissolve the entire crystal, bilayer by bilayer at the time. Assuming ideal stoichiometry, the reaction is given by:

$$2GaN + 3H_2O \longleftrightarrow Ga_2O_3 + 2NH_3 \tag{2.3}$$

Contrarily, on a Ga-polar (0001) surface, strong repulsion occurs between OH^- and the three negatively charged dangling bonds of N atoms, forming an etch-stop after removal of the outer most Ga layer [24].

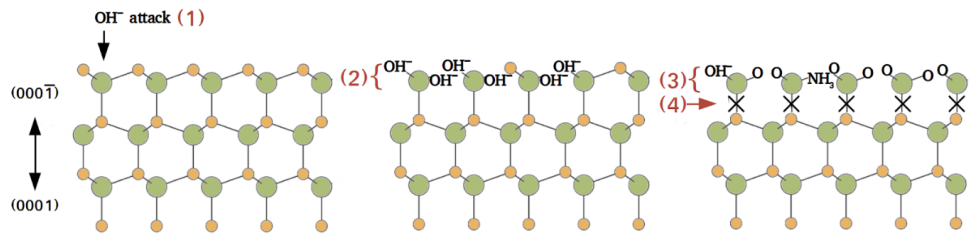

Figure 2.7: (a) Schematic representation of the selective wet etching of N-polar GaN in hydroxyl solution, modified from [24].

In Paper I, N-polar inversion domains in Ga-polar GaN are revealed by etching in a solution of molten NaOH at 70° C. The sample consists of a coalesced GaN nanowire array (growth is summarized further below) with clearly visible GaN cores (dark hexagons), as shown in Fig. 2.8. A foliated configuration with different etching steps is highlighted in the inset of Fig. 2.8. The self-limiting nature of the etching process is confirmed by prolonged etching time, when exposed IDs are removed.

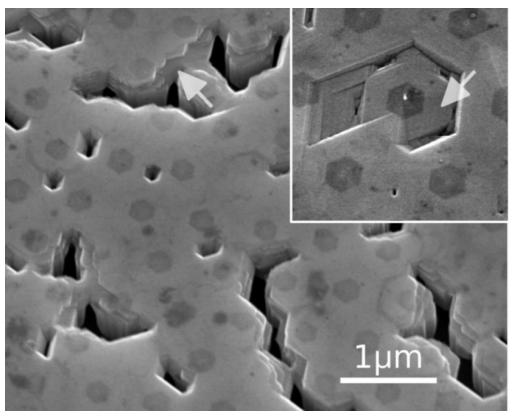

Figure 2.8: SEM image of a GaN surface upon removal of N-polar domains by NaOH.

2.3 Crystal growth

In most basic form, epitaxial growth is the crystal growth that continues the atomic arrangement and crystallinity of a crystal seed often refereed to as the substrate. This is in contrast to e.g. sputtering or deposition techniques, that result in amorphous layers or polycrystalline structures independent of the crystal direction. Some of the major techniques for epitaxial growth semiconductor materials and layers are liquid phase epitaxy (LPE), metal organic vapor phase epitaxy (MOVPE), and molecular beam epitaxy (MBE). These methods differ in utilization of thermodynamic phase transitions, material diffusion, kinetics, surface energies, etc. The choice of the growth technique will depend primarily on the kind of semiconductor structure fabricated. LPE utilizes high temperatures to grow high quality material from a melt, using a crystal seed as substrate. The growth is done homopeitaxially, meaning that the grown crystal is of the same material composition throughout. LPE, which is working close to thermodynamic equilibrium, is mainly used for fabrication of base material ingots, for semiconductor substrates. It is not possible to grow III-nitrides by pure LPE (only melt of the crystal material) mainly because the III-N nitrides do not melt into liquid form but dissolve into their constituents, where N_2 remains inert over a massive range of conditions. As example, it has been shown that GaN requires 2700° C in combination with a pressure of 6 GPa to form a congruent melt [25]. This leaves the extremely challenging task to develop III-nitride bulk substrates by alternative approaches, such as high vapor pressure epitaxy, ammonothermal growth and high pressure solution growth [26] while fabrication of large scale substrates are fabricated by MOVPE through heteroepitaxy on foreign substrates.

2.3.1 Metal organic vapor phase epitaxy

The compound III-V semiconductors presented in this work were grown by MOVPE, which utilizes a gaseous flow with precursors mixed with an inert carrier-gas. The precursors are molecules comprising the crystal source-atoms. For the source atoms to precipitate into epitaxial layers on the substrate the precursors must diffuse to the substrate-surface and decompose there, through a process called pyrolysis. The temperature required for pyrolysis depends on the required energy to break the bonds of the precursor molecules but is also influenced by catalytic effects at the substrate surface.

MOVPE generally uses high V-III ratios. For MOVPE of conventional III-Vs, the precursors should preferably satisfy the following requirements: 1) they must dissociate at 500-800 °C, and 2) they must be gaseous or have high vapor pressure at room temperature. For the III-nitrides, the conditions are different. In order to dissociate the group-V precursor (NH_3) efficiently, temperatures above 1000°C are often required, however, decomposition temperature of GaN is below 1000°C (sublimation temperature at atmospheric pressure is

about 850°C). This means that the nitride would start outgassing. To correct for this and relatively low vapor pressure of NH_3, even higher V-III ratios are needed than for conventional group III-V semiconductors. The group III precursors most usually comprise alkyls, which have a relatively high span of vapor pressures, with ethyl based precursors, such as tri-ethyl gallium (TEG), at the lower range limiting their achievable flow rate.

MOVPE, being a gas phase epitaxial technique involves a mix of several mechanisms relevant for growth. Among the critical, often simultaneous, mechanisms are 1) fluid dynamics of the incoming precursors, simultaneous with 2) pyrolysis and competing parasitic reactions, 3) the last stage of gas phase transport to the crystal surface which only is diffusion limited through a gas layer above the surface called stagnant layer. 4) When the sources have reached the crystal surface, pyrolysis, crystal growth kinetics and atomic surface diffusion are into play [27]. In addition there is forced convection due to the forced flow between inlet and outlet, and free convection due to the temperature gradient at the sample.

Design of an MOVPE requires minimization of areas having very small or no gas velocity, termed dead volumes. Similarly, the operation at low pressures can be beneficial, since it enhances the viscous gas-flow, reducing dead volumes within the reactor. Dead volumes are potential traps for trace gases, that may be released over time, resulting in unwanted changes in doping or composition, known as memory effects, which may lead to gradient transitions between layers and may also result in background doping in layers that are intended to be intrinsic.

Some materials are more prone to giving memory effects, since they have relatively high vapor pressure and will stick to walls at dead volumes. This is a challenge for some dopants like Zn and Mg, while Si, with low vapor pressure, is quite unproblematic. Of the group V-sources, phosphine (PH_3) with pyrolyzed byproducts have a comparably massive vapor pressure, and also the vapor pressure of arsine (AsH_3) with byproducts is very high. That's why one never combines nitride growth with conventional III-Vs in an MOVPE reactor. NH_3 with byproducts have a low vapor pressure and if AsH_3 or PH_3 is introduced into the chamber pure GaN growth will be off the shelf.

For epitaxially grown III-V materials, fabrication of *n*-type and *p*-type layers is typically done through impurity doping during epitaxial growth, by MOVPE precursors dedicated for doping. Post-growth doping, by diffusion or ion implantation can also be used but is much more common in processing of elemental semiconductors. In MOVPE, the process of doping may be challenging since the concentrations required are low while the dopant is objected to the same multitude of mechanisms involved for other sources. To estimate incorporation during growth can be hard, as it depends on arrival rate and surface mechanisms like re-evaporation and incorporation. Gas phase pyrolysis with parasitic reactions may render a metal organic dopant source inefficient, and as mentioned above memory effects may be severe. This is less of a problem for planar layers, where control measurements

like secondary ion mass spectroscopy and Hall voltages can be used to fine tuning doping levels but remains a challenge for nanostructures.

2.4 Nanostructure growth

This work encompasses characterization and analysis of a selection of nanostructures, semiconductor materials, and epitaxial growth methods. First, growth of In(Ga)P nanowires by the vapor liquid solid (VLS) method is discussed. Then selective growth of GaN nanowires and, further, the selective growth of III-N nanostructures are discussed. The latter highlights the growth of 1) GaN NWs with InN quantum dots and 2) InGaN platelets with InGaN quantum wells. Finally, the process of reformation of a GaN NW array to form a GaN substrate, going from nanostructure to macroscopic material, is presented.

2.4.1 Vapor liquid solid growth of nanowires

The VLS growth mechanism [28] as illustrated in Fig. 2.9 is often used to grow NWs. The anisotropic growth is enabled by catalytic particles (a) where growth is enhanced at the particle/crystal interface. The most common particle material used is Au, which forms an eutectic melt together with the group III materials, so that the alloyed Au/group III particle may be in liquid form at growth temperature. The particle acts as a sink for precursors, (b). Precursors preferentially arrive at the droplet, decompose, and dissolve in the catalysis leading to supersaturation of the molten eutectic. The supersaturation facilitates axial growth of nanowires (c), allowing crystallization of a solid within the melt-solid interface. The nanowire length, width, and shape will be governed by this process [29], mainly by the growth conditions such as growth time, temperatures, precursors choice, etc. (d). In addition, the spacing, location, and diameter of liquid metal droplets will also influence the vertical and radial growth of NWs. Introducing different precursors and changing the growth conditions allows formation of axial and radial heterostructures (e) [30].

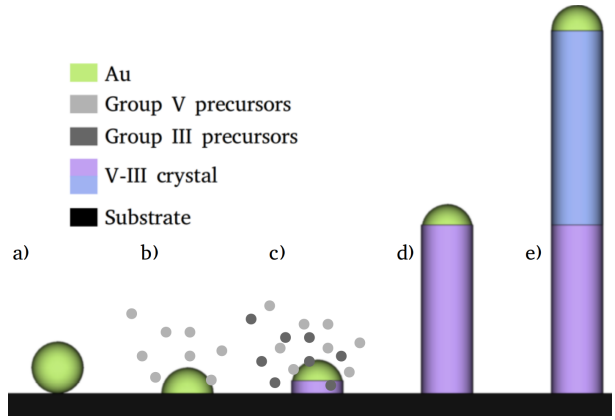

Figure 2.9: Synthesis of nanowires by VLS highlighting the catalytic particle on a substrate (a), alloy formation (b) with group V precursors, introduction of group V and III precursors resulting in nanowire growth (c). (d-e) Introduction of dopants during growth allows formation of axial junctions (d-e).

Growth of In(Ga)P NW arrays

The In(Ga)P nanowires investigated in this thesis (Papers VI and VII) were grown epitaxially using Au-assisted VLS by MOVPE. The processing and growth sequence of InGaP and InP nanowires follows below. Substrates with lithographically defined gold particles were used. The samples were annealed in a phosphine atmosphere, then the precursors trimethylindium and trimethylgallium were led into the reactor to initiate NW growth. The NWs were grown with an axial *p*-*i*-*n* junction, containing *p*-type, *i*- intrinsic, and *n*-type segments. The *n*-type dopant was Sn, using tetraethyltin as precursor, while Zn was the *p*-type dopant, using diethylzinc. The choice of doping precursors is especially sensitive for NW growth, since they may influence and axial growth rates, alter composition and solubilities in the catalytic particle, and even influence crystal structure. An excellent review on doping of NWs can be found in [31]. The resulting array of NWs is shown in Fig. 2.10.

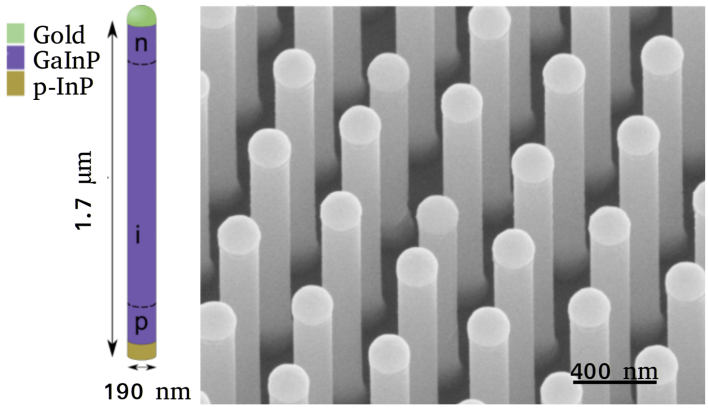

Figure 2.10: Sketch and SEM image of an InGaP NW array, image courtesy of Vilgaile Dagyte.

2.4.2 Selective growth of III-N nanostructures

While it's possible to nucleate (Al)GaN nanowires spontaneously by MBE, more deliberate approaches are required in MOVPE. Selective growth is such a method which can provide GaN NWs grown in predefined patterns and which results in arrays with excellent homogeneity, making it well suited for large scale production.

As indicated by its name, selective growth utilizes the mobility of surface ad-atoms and the use of metal organic precursors to only grow at certain areas, or even facets, which makes it unique for MOVPE and CBE (chemical beam epitaxy). There is a distinction between growth confined to open substrate areas in a mask-pattern, called selective area growth (SAG), and selective growth on certain facets, often referred to as selective surface growth (SSG). This distinction is not always clearly made though.

The GaN NWs presented in this dissertation utilize both SAG and SSG. The apertures in a dielectric mask provides selective area growth, exposing an underlying GaN crystal and allowing epitaxial nucleation of nanowires. Selective surface growth is utilized in the anisotropic growth rates in NW growth, with high growth rate in the (0001) direction but essentially no lateral growth on the $(10\bar{1}1)$ side facets.

There is an interplay between the spacing and hole size in the lithographically patterned mask, these two parameters results in different nanowire vertical growth rate and must be adapted appropriately. The trend is as following: larger pitch and smaller apertures result in longer nanowires, and vice versa.

GaN NWs with InN QDs

Growth conditions that promote vertical GaN NW growth must generate a high Ga surface mobility at the side facets in comparison to the end of the NW. The Ga precursors and NH_3 are used at low V/III ratios, which may advantageously influence the surface reconstruction of dangling bonds on the different surfaces, but will also limit the influence of the nitrogen source on the surface mobility of the Ga precursors/atoms, such that they diffuse along the *m*-plane to precipitate at the top of the NW. This results in a nanowire core having six $\{10\bar{1}0\}$ *m*-planes, a flat (0001) *c*-plane, and six inclined $\{1\bar{1}01\}$ facets at the top, as shown in Fig. 2.12(b).

In Paper V, we present GaN nanostructures with active regions in form of InN quantum dots (QDs) for potential opto-electronic device application. The QDs are formed by the Stranski Krastanow (SK) method where growth of a thin lattice-mismatched layer above a certain critical thickness results in the transformation to QDs when grown above the certain critical thickness. SK can be formed with impressive homogeneity in size and distribution [32], but is very sensitive to irregularities on the surface, such as dislocations. Therefore, the NWs' symmetric configuration of flat dislocation-free $\{10\bar{1}0\}$ side facets are attractive prospects as templates for SK-growth of QDs.

InN SK-dots were grown on GaN NWs in MOVPE reactor. The GaN NW growth was realized using a SiN mask fabricated onto a GaN/Si substrate. Pattern of aperture in the SiN mask was fabricated by electron-beam lithography (EBL) and reactive ion etching (RIE), resulting in 100 nm diameter openings. GaN NWs were grown with a low V/III ratio of 11 in TEG flow of 19 μm/min and the temperature of 1042 °C. After NW growth, the V/III ratio was increased to 7000, initializing lateral growth, resulting in 400 nm wide NWs. The dependence of InN SK-dots formation on growth parameters were investigated by altering growth temperature and source flows (600-730 °C, TMI (6-33 μm/min), and NH_3 (100-300 μm/min)). It was shown that higher growth temperatures lead to an increased diffusion length and a reduced QD density. Over 730 °C, QDs couldn't be formed due to decomposition of InN and desorption of In. It was also shown that InN QDs could be formed either on edges or on the *m*-planes by controlling adatom or precursor migration. These results correlate well with SK growth using conventional III-Vs [32]. However, the InN QDs where found to comprise regularly distributed I1 type stacking faults and a *c*-plane crystal tilt to accommodate the high strain. This may explain the low optical output of the QDs.

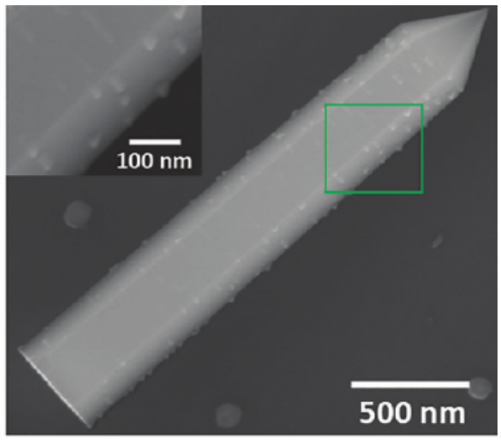

Figure 2.11: GaN nanowire with InN QDs, from Paper V.

Planarization of III-N NWs

As discussed previously in this chapter, fabrication of high-quality large scale GaN wafers remains an unsolved problem. Paper I and II focus on surface characterization and analysis of a novel epitaxial approach to this challenge and the resulting GaN substrate. In short, the method utilizes the dislocation filtering abilities of selectively grown NWs and the subsequent coalescence of these nanostructures by reformation instead of conventional lateral overgrowth by MOVPE.

The method, as shown in Fig. 2.12, comprises selective growth of a homogeneous array of GaN NWs (a), then uniform shell-growth was promoted by increasing the V/III ratio (b). Growth of the tilted $\{10\bar{1}1\}$ facets is slow, due to their high surface energy, leading to a pyramidal nanostructure, as can be seen in (c). This step was continued until the *m*-planes of neighboring NWs was approximately 50 nm apart.

Coalescence of the GaN NW core-shell structures is achieved by reformation, a process at which the Ga precursors is entirely shut off and only a background flow of (NH_3) is used, resulting in a zero net growth. This step requires a temperature where Ga atoms can dissociate from their crystal site but still not desorb from the surface. Instead, they rearrange, as adatoms, driven by the difference in surface energy between facets, enlarging lower energy facets and decreasing the area of higher energy facets. The process results in a surface as the one shown in Fig. 2.12 (d). The contrast difference between NW core, shell, and coalesced material is apparent in the SEM top view image. More details about the growth can be found in the publications (Paper I and II).

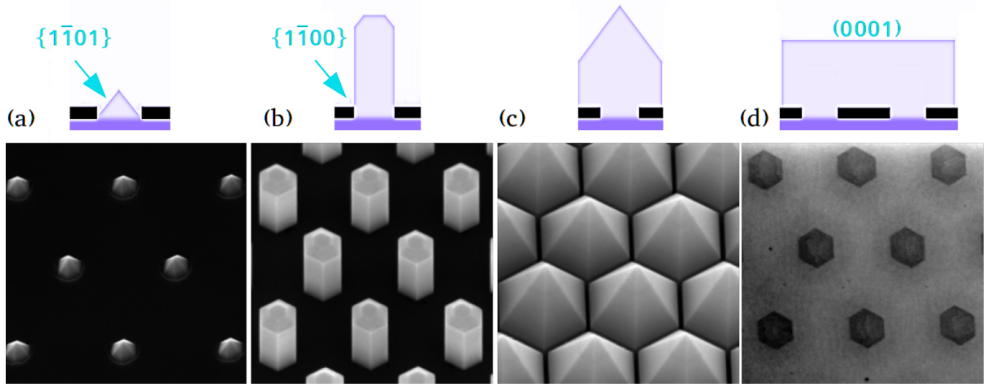

Figure 2.12: Schematics (top) and SEM images (below) of four crucial steps in NW growth: (a) nucleation, (b) vertical and (c) lateral growth, and (d) reformation resulting in a thin continuous film.

InGaN platelets with QWs

By changing the amount of In in InGaN, the band gap can be altered to fabricate quantum wells in micro-LED structures adapted to emit red and green and blue light. This is important, since it allows lighting based on fabrication of RGB LED lamps but also for fabrication of RGB displays. Here the growth process of InGaN nanoplatelets is presented along with subsequent growth of a *p*-*n* junction within a quantum well to form an LED, addressed in the following chapter. By nanoplate geometry we typically refer to the shape in the form of truncated pyramids, dominated by the semipolar {10$\bar{1}$1} side facets and the polar (0001) facet.

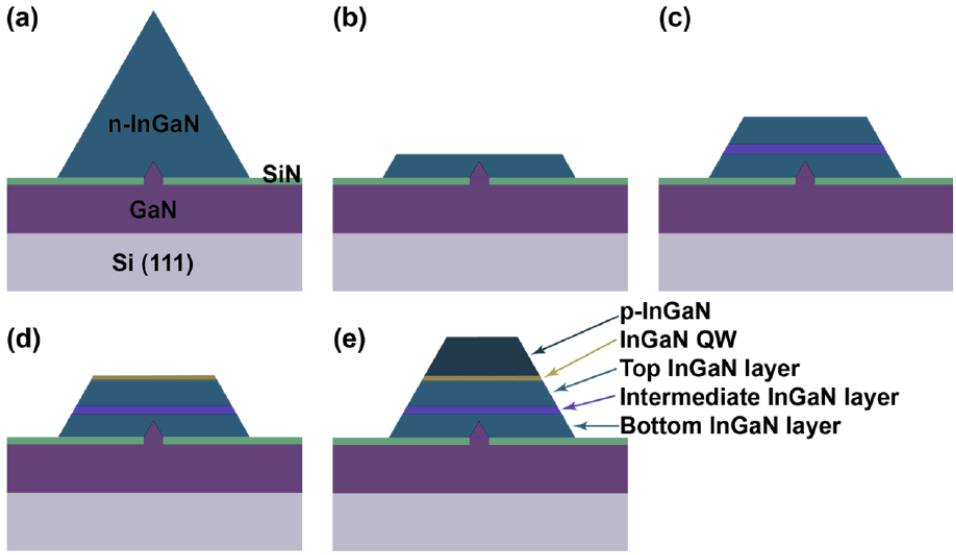

Figure 2.13: Illustration of the growth and formation of InGaN platelets and LED structure. (a) shows *n*-type InGaN formation by MOVPE growth, (b) the bottom InGaN layer formed by *in — situ* annealing, (c) Regrowth results in an intermediate layer. (d) Step (b) is repeated resulting in the formation of a top InGaN layer. Finally (e) shows a schematic of our prototype LED structure with a *p*-InGaN layer grown on top of a single QW, from Paper III.

InGaN growth is typically carried out with N_2 as carrier gas, since H_2 is known to increase the dissociation rate of In. Growth of the $\{10\bar{1}1\}$ facets is comparatively slow, leading to a pyramidal shape, see Fig. 2.13(c). The *n*-type dopant is Si, using SiH_4 gas as precursor. *p*-type InGaN is achieved by Mg doping, using bis(cyclopentadienyl)magnesium (Cp_2Mg) as precursor. Typically, Mg is a semi shallow acceptor impurity in GaN, forming a level around 220 meV [33, 34, 35] above the valence band, therefore, at room temperature, the ionization rate is rather poor. However, the acceptor level becomes more shallow with increased In composition in InGaN. Further details of the growth can be found in paper III.

In paper IV, a different approach to synthesizing InGaN template was devised. Here, after the InGaN pyramids were grown, same as in Paper III, a layer of SiO_x was deposited over the sample by plasma enhanced CVD. Chemical mechanical polishing (CMP) was then used to polish the wafers, exposing the *c*-facets. HF was used to etch away the remains of SiO_x. The obtained *c*-plane was curved, and the flattening achieved by further growth at NW growth conditions.

Chapter 3

Nanostructure devices

Due to their ability to relax the strain around their periphery, high quality NWs can be grown with well defined core/shell radial heterojunctions along with vertically stacked axial heterostructures. Increased elastic relaxation at the lateral free surface [36] means that we may fabricate quality heterostructures between semiconductors which are not perfectly lattice-matched, allowing us to work with a larger range of semiconductor alloys and band-configurations. Ultimately, it may also provide means to grow dislocation free, single crystal material on cheaper, and less perfect, substrates. The following chapter introduces *p*-*n* junctions heterostructures for nanowire-based solar cells and LEDs.

3.1 The *p*-*n* junction

Diodes are devices that only allow current to flow in one direction. *p*-*n* diodes are semiconductor rectifiers which can be used to construct efficient light emitters (in LEDs) and solar cells (in photovoltaics). The basic structure of a diode is a junction between a *p*-doped and an *n*-doped semiconductor. As discussed in chapter 2, a *p*-type semiconductor is doped with acceptor impurities, providing a large concentration of positively charged holes in the valence band while an *n*-type semiconductor, doped with donor impurities, will have an excess of negatively charged electrons in the conduction band. The dominant charge carriers in the semiconductor are called majority carriers, whilst the less abundant are termed minority carriers. Since some electron states of the conduction band are filled in an *n*-type semiconductor, the Fermi level is close to the conduction band. By the same reasoning it is clear the Fermi level will be lower in a *p*-type semiconductor, since there are empty electron states (holes) in the valence band. In thermodynamic equilibrium the Fermi level must be equal in the whole system. When the *p*- and the *n*-type semiconductors are brought

together, majority carries diffuse from the junction, leaving uncompensated donor and acceptor ions in a region depleted of charge-carriers, called space charge region (SCR), or the depletion region, resulting in an electric field and therewith a built-in potential across the SCR region, resulting in band bending. This potential difference can be altered by external voltage resulting in a change in a width of the depletion region. A diode is said to be reverse biased when the n-side is connected to the positive terminal. This will result in an increase of built in potential (widening of the SCR region), and the energy required for diffusion of majority carriers will be too high, resulting in a negligible current flow. Forward biasing a diode will lower the electrostatic potential of the *p*-*n* junction, counteracting the built in potential barrier allowing the majority carriers with sufficient thermal energy to surmount the lowered barrier. As the bias is further increased, diffusion current will increase exponentially. The resulting current-voltage (*I*-*V*) relation of the diode is:

$$I = I_S(exp\frac{eV}{nk_B T} - 1) \tag{3.1}$$

where I_s is the dark saturation current, e is the elementary charge, T is the temperature, k_B is the Boltzmann constant, and n is the ideality factor, ranging from $n = 1$ to $n = 2$, where $n = 1$ represents the ideal diode curve. The current-voltage (*I*-*V*) characteristic curve is shown in Fig. 3.2 (dashed line), with exponential *I*-*V* dependence in the forward direction and current-blocking in reverse bias. Plotting the diode curve of Eq. 3.1 in logarithmic scale, it becomes clear that the *I*-*V* slope gives e/nk_BT, from which n can be obtained, and the intercept gives $ln(I_s)$.

3.2 Solar cells

3.2.1 Principle and photovoltaic figures of merit

The basic operating principle of a solar cell is illustrated in Fig. 3.1. The solar cell is based on a *p*-*n* junction designed and optimized to transform photon radiation of the sun to electrical energy. Electron-hole pairs are generated when photons, with energy larger than the band gap, are absorbed. When electron-hole pairs are generated in the depletion region, the built-in field of the depletion region separates them, generating a drift-current. An external current is realized through diffusion of majority carriers in the *n*- and *p*-regions to an external circuit, providing electrical power.

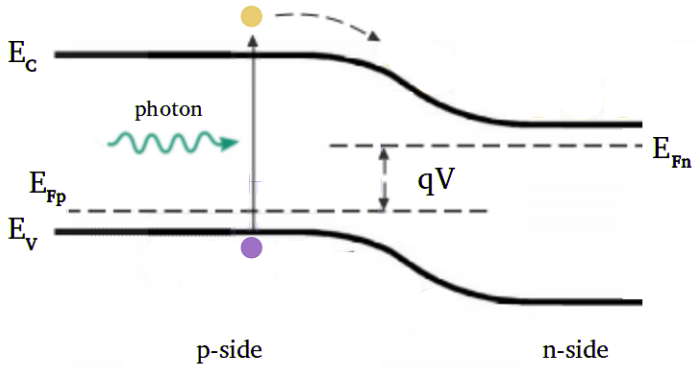

Figure 3.1: Sketch of band diagram of a solar cell under illumination. The injected photons excite pairs of charge carriers that get separated, resulting into a separation (qV) of the Fermi level into two quasi-Fermi levels.

This process results in a photocurrent, I_{ph}. By the use of superposition, the current behavior of the solar cell, I_{light}, is the sum of I_{dark} (I in Eq. 3.1) and I_{ph}:

$$I_{\mathrm{light}} = I_{\mathrm{s}}(exp\frac{eV}{nk_{\mathrm{B}}T} - 1) - I_{\mathrm{ph}} \tag{3.2}$$

The current voltage ($I - V$) characteristics of a *p-n* junction solar cell under illumination (solid line) is superimposed to a dark current (dashed line), in Fig. 3.2.

Parasitic recombination is a typical problem in solar cells, and the ideality factor provides the information on where the recombination occurs, e.g., recombination in quasi-neutral regions gives a rise to diode current $n = 1$, while recombination in the depletion region gives $n = 2$. Typically n lies in between these two values, depending on the relative weights between the two mechanisms.

Two extreme points, short circuit current I_{sc} (current at 0 V) and open circuit voltage V_{oc} (voltage at 0 current), are marked. Assuming the exponent in equation 3.2 is much larger than 1, it follows:

$$V_{\mathrm{oc}} = \frac{nk_{\mathrm{B}}T}{e} ln\frac{I_{\mathrm{sc}}}{I_{\mathrm{s}}} \tag{3.3}$$

At V_{oc} and I_{sc} the power delivered by a diode is zero, meaning that the solar cell should be operated in between these two points, where the maximum power is defined as

$$P_{\mathrm{out}} = \frac{I_{\mathrm{sc}}}{V_{\mathrm{oc}}} FF = I_{\mathrm{mp}} V_{\mathrm{mp}} \tag{3.4}$$

determined by fill factor (FF), in conjunction with V_{oc}, and I_{sc} or at maximum voltage and current (V_{mp} and I_{mp}). In Fig. 3.2, FF is a measure of the "squareness" of the solar cell, the area of the rectangle bounded by V_{oc} and I_{sc}.

This condition means that there is an optimum band gap for a single junction solar cell, given by the black body solar spectrum . We want to absorb as many photons as possible to raise I_{sc}, since photons with energy below the band gap are not absorbed. Consequently, a low band gap solar cell will absorb a larger fraction of of the photons of the solar spectrum. At the same time, we want a high band gap in order to raise V_{oc} but the photon energy above the band gap energy will be lost to thermalization during electron relaxation back to the band edge. This means that, ideally, ignoring any other effects, the optimal band gap would be given by the I_{mp} and V_{mp} that gives the largest product, P_{out} from our sun's spectrum.

To optimize the solar cell performance a parasitic recombination must be understood and minimized. Generation of minority carriers by photon absorption in the p- and n-regions invites parasitic recombination of the majority carrier, or they may diffuse to the back contact, decreasing efficiency in both case. The cell must be engineered properly, so that most of the minority carriers are diffused through the junction and collected. Some of the major ways to minimization of recombination rate include: 1) higher quality material with high diffusion coefficients, 2) thinner base layer, but optically thick enough to trap all photons, 3) engineering the cell such that the photons are absorbed in depletion region where the built in electric field pushes them towards their majority-region, 4) reducing the contact area, which may cause carrier recombination through high defect density.

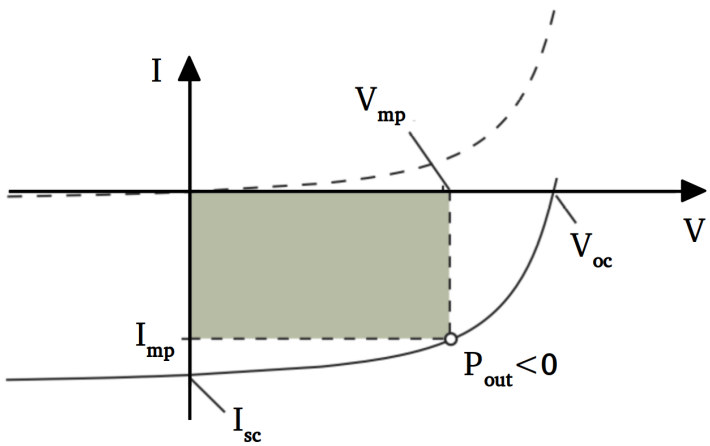

Figure 3.2: Current-voltage characteristics of a *p-n*junction solar cell in dark (dashed) and under illumination (solid line). Maximum power delivered by a solar cell is depicted with the green rectangle.

3.2.2 In(Ga)P nanowire based solar cell

The relaxed constraints of the NW geometry, allows growth of lattice mismatched materials, in contrast to traditional planar structures. This offers 1) more freedom in choice and

combination of nanowire materials, and 2) epitaxial growth on a cheaper substrate. Other advantages of the nanowire geometry include the ability to tune the nanowire diameter, length, and filling ratio for a specific wavelength to allow strong absorption of sunlight while using small volume of the material [37, 38]. Furthermore, by embedding the nanowires in a polymer and peeling them off, the original growth substrate can be reused [39].

The InP material system is characterized by a relatively low surface recombination velocity [40], efficient charge separation, and a direct band gap of 1.34 eV, being essentially the optimal band gap for a single junction solar cell. The growth of InP nanowire solar cells is facilitated by its compatibility with *in situ* HCl etching [41], to eliminate radial overgrowth, short circuit paths, and recombination centers at the surface. To date, InP NW based solar cells provide a record efficiency of 15 % [42] (for bottom-up approach) and 17.8 % [43] (top-to-bottom), while electro-optical modeling shows possible reach of efficiencies up to 32.5 % [44].

One way to boost efficiency is through a tandem solar cell geometry, where a high band gap III-V combination is epitaxially grown as on top of a low bandgap material, to match two segments of the solar spectrum. A curious reader may find guidelines for achieving higher efficiencies in [45] and an in-depth study on InP nanowires in [31].

3.3 Light emitting diodes

3.3.1 Radiative recombination

Just like the solar cell, the LED is an optoelectronic device based on a *p*-*n* junction. However, while electron-hole pair recombination is a source of loss in the solar cell, the LED is designed, materials selected, and arranged, to aid the emission of photons by radiative electron-hole recombination. This in contrast to non-radiative recombination, which does not result in a photon emission. The wavelength of the emitted photon is defined by the band gap. Consequently, an efficient LED requires a direct band gap, its energy corresponding to the wavelength of the intended light output.

3.3.2 Mechanisms of the LED

Forward biasing the *p*-*n* diode enhances diffusion of electrons and holes into the depletion region where they can recombine. To increase the efficiency of recombination, an active region, comprising of one or more quantum wells (QWs) with smaller band gap than the surrounding *p*- and *n*-regions, is typically placed in the depletion region, as shown in Fig. 3.3. Ideally, the thickness of the QWs should be of the same order as the electron and

hole diffusion lengths, thereby allowing efficient radiative recombination of the electron-hole pairs. However, the diffusion lengths of electrons and holes are often highly disparate, especially so in III-Vs and III-Ns. In Fig. 3.3 *p*-AlGaN is added as an electron blocking layer to retain the highly mobile electrons in the active region, even at high-level current injection [46].

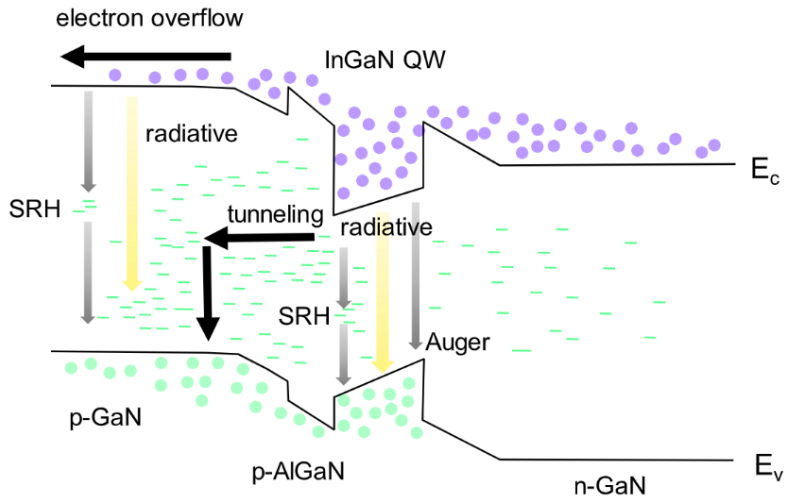

Figure 3.3: Schematic illustration of InGaN based LED illustrating radiative and nonradiative processes. The junction is formed by *n*-GaN, active InGaN layer, *p*-AlGaN, and *p*-GaN, modified from [47].

3.3.3 Loss and nonradiative recombination

The AlGaN electron barrier of the example structure in Fig. 3.3 also prevents overshoot of electrons into the *p*-region, which would result in unwanted electron-hole recombination in the *p*-region, essentially decreasing hole injection into the active region. Such behavior is called as a shunt leakage effect, although it involves recombination.

Ignoring resistive losses and leakage, the efficiency of a LED can be expressed as its quantum efficiency, defined as the ratio of the radiative recombination to the total recombination rate [47].

One form of non-radiative recombination is trap assisted, prominent in materials with high density of defects, e.g. III-nitrides. A defect-induced energy state in the band gap of the active layer (QWs) may capture delocalized electrons or holes, which thereby are falling short from the emission of photons. This process is known as Shockley-Read-Hall (SRH) recombination process. Even if this capture process is radiative, resulting in radiative electron-hole-pair recombination, it is still considered a loss, since the photon wavelength will be shifted. The radiative capture is slow, and shown to not be detrimental to devices.

Another example of a non-radiative electron-hole recombination process is Auger recombination where excess carrier energy excites a third carrier to a higher energy level within the same band. The excited carrier thermalizes back close to the band edge. Auger recombination results in reduction of luminescence efficiency at high carrier concentration, caused either by heavy doping or high-level injection currents. The probability of Auger recombination rate decreases with an increase in band gap and decrease in operating temperature [48].

3.3.4 Polarization in nitride LEDs

The InGaN alloys certainly satisfy LED requirements, having direct band gaps, spanning the entire visible range. Blue LEDs, used for lighting applications (LED lamps) are GaN pn-junctions with InGaN active layers, see Fig. 3.3.

However, there are a number of challenges that need to be addressed, two of them being spontaneous and piezoelectric polarization (see also chapter 2.1).

Spontaneous polarization (composition driven) is found in non-centrosymmetric crystals, and piezoelectric polarization is driven by the offset in charges as a result of strain, see chapter 1. Polarization results in fixed charges and strong internal electric fields across quantum wells, in direction towards the III-polar surface. This leads to a tilted potential profile, spatial separation and less overlap between the electron and hole wave functions, see Fig. 3.4(a). In order to keep a high radiative recombination rate the QW must be thin, typically below 3 nm, so that overlap of electron and hole wavefunctions still is retained [49]. As previously discussed, a thin QW means increased probability for electron overshoot. This is typically accommodated by an active region comprising a multi-quantum well (MQW) structure together with the previously discussed electron blocking layer, Fig. 3.3. This restriction can also, theoretically, be relaxed by choosing a semipolar direction, or completely removed by growing in an nonpolar direction, Fig. 3.4(b). In optoelectronic quantum structures, this strong polarization induced electric field on polar planes is known as the quantum confined Stark effect (QCSE) [47]. QCSE is increased if the composition difference between the well and the barrier is increased, as this will increase the strain and polarization induced electric field in the QW further. Recent research has correlated increased QCSE with earlier onset of auger recombination and droop [50], suggesting that high efficiency is pendant on QW/barrier structures close in composition.

3.3.5 InGaN nanostructure-based LEDs

An InGaN QW grown on *c*-plane GaN is common choice for the active layer in an LED design, see Fig. 3.3. While the highly efficient blue $In_{0.15}Ga_{0.85}N$/GaN LEDs was the

cornerstone for the transition to LED based lighting, green and red InGaN/GaN LEDs, requiring QWs with approximately 35 % and 25 % In concentration, remain a challenge. One reason is certainly the high compositional difference of $In_{0.25}Ga_{0.75}N$/GaN and $In_{0.35}Ga_{0.65}N$/GaN LEDs, resulting in plastic deformation, extreme QSCE and, plausibly, early onset Auger recombination. It's easy to imagine the possible advantages of high quality InGaN substrates. While such substrates are unavailable, we can try to make InGaN nano templates. This approach may also facilitate further challenges that need to be addressed in InGaN growth, namely In pulling and *p*-type doping.

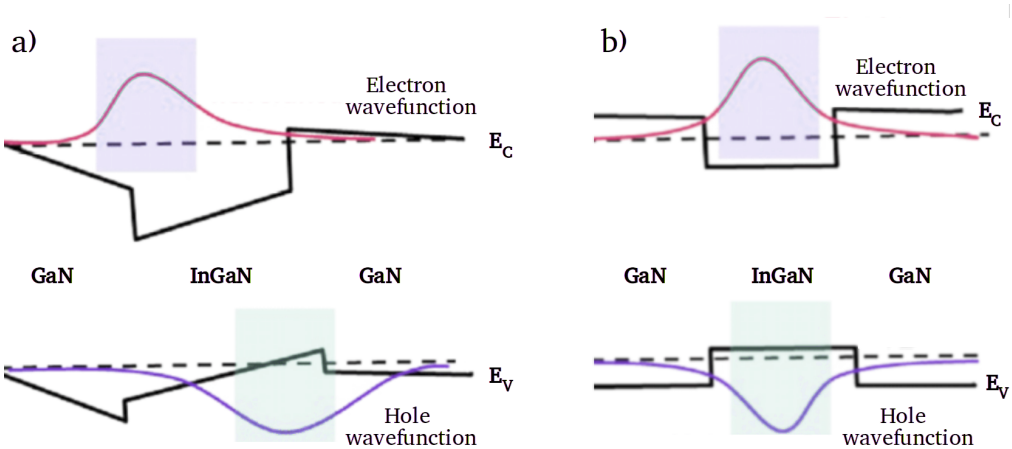

Figure 3.4: Schematic of band alignment of an InGaN QWs for (a) polar and (b) semi/non polar surfaces, modified from [51].

An $In_{0.2}Ga_{0.8}N$ film grown on GaN has an around 2 % larger in-plane lattice constant [4]. The large difference in interatomic spacing leads to phenomena called composition pulling [52]. The pulling effect leads to increasing In composition with the layer-thickness. Furthermore high density of point and structural defects introduce states within the band gap and hence increase the probability of non-radiative recombination mechanism. The InGaN film may have decent crystalline quality near the InGaN/GaN interface, getting progressively worse, degrading into a surface with non-uniform, In rich islands.

The above challenges can be facilitated by opting for nanostructured LEDs. First, the small footprint allows filtering of structural defects originating from the substrate below, as discussed in Papers I-V. The small footprint of the GaN seed also allows for mismatched growth of high quality InGaN structures by elastic strain relaxation. Second, different facets are available, possibly allowing QWs to be grown on non-polar planes, thus reducing or removing completely spontaneous polarization effects. Third, traditional *c*-plane LEDs can be fabricated with low compositional InGaN QW/InGaN barrier difference, similar to high efficiency Ino.15Ga0.85N/GaN LEDs, enabling red-green-blue LEDs from the same material family, by varying In-Ga ratios.

In Paper III, we reported on the prototype InGaN platelet green and red LEDs with a full width at half-maximum of photoluminescence of 107 and 151 meV for 9 and 18 % In, respectively. In Paper IV, we reported a growth of high quality, dislocation free, InGaN platelets with an In content of 17-18 %. Photoluminescence showed a full width at half-maximum of 140 meV at 2.63 eV. Compared with the work reported in Paper III, we show that the platelets are dislocation free. The growth of these structures was introduced in chapter 2.

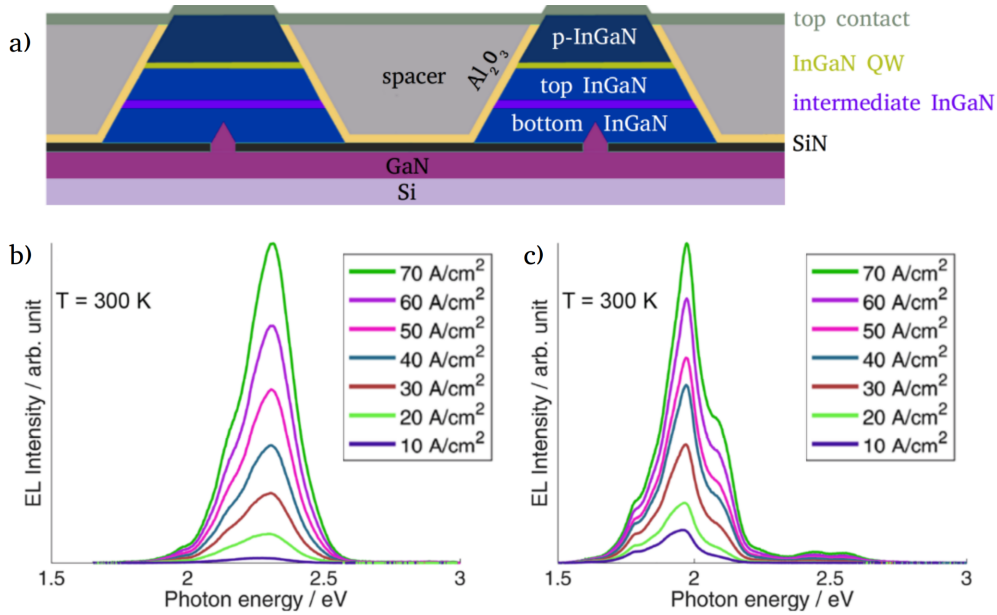

Figure 3.5: (a) Schematics and (b, c) electroluminescence measurements of prototype InGaN platelet LED. Electroluminescence spectra obtained for In concentrations of (b) 9 % and (c) 18 %, modified from Paper III.

Figure 1. Procedures to synthesize InGaN platelets and LED structures. (a) InGaN pyramids grown by selective area MOVPE, as reported in an earlier work.29 (b) Bottom InGaN layer with a top c-plane formed by etching down from the pyramid apex using in situ annealing. (c) InGaN regrowth to flatten the rough c-plane formed in panel b. An intermediate layer of InGaN is grown first with an indium content of <5Figure S1 in the Supporting Information. Then, a top InGaN layer is grown with an indium content similar to that of the bottom InGaN layer in panel b. (d) InGaN single QW growth on the c-plane of the InGaN platelet templates. (e) Prototype LED structure with p-InGaN grown above the single QW, with definitions of all InGaN layers.

Chapter 4

Scanning probe techniques

Two characterization techniques were implemented heavily during this dissertation, namely, atomic force microscopy [53] (AFM) and scanning tunneling microscopy [54] (STM). Although they are based at the same operating principle, that is, raster scanning sharp probe tips in close proximity over sample surfaces and measuring the different tip-surface interactions, the type of interaction required to build an image is unique to build an image, are unique to each technique. For the STM, the interaction is based on electron tunneling between a metallic tip and a conductive surface through a vacuum gap allowing simultaneous study of the structure and electronic density of states. To the contrary, the AFM probes the interaction forces that the tip feels as it is rastered over the surface. In a sense superior, the AFM provides true physical height and at the same time overcomes the need for a conductive sample. Moreover, by modulating the AFM instrumentation components, a powerful family of microscopes capable of measuring simultaneously topography and local current (conductive-AFM), (local) work function [55] (Kelvin probe microscopy), and doping type and carrier concentration [56] (scanning capacitance microscopy) has been developed, all of which have been used during this thesis work The following chapter is meant to provide fundamentals of above mentioned techniques and connect them to the results presented in my papers. For a more in depth discussion a reader will be provided with references for an extended review on the subject at appropriate times.

4.1 Atomic force microscopy

4.1.1 Tip-surface interaction forces

The AFM is based on tip-sample interaction forces $F(d)$, which are utilized by the feedback system for generating an image. These forces vary in type with the tip-sample distance, as shown in Fig. 4.2(c). The interaction can be in the most general way modeled by the Lennard-Jones potential by a first order approximation of a single atom termination both at the tip apex and the surface. The Lennard-Jones potential, $U(d)$, is given by the empirical atom-atom interaction:

$$U(d) = 4\epsilon \left[\left(\frac{\sigma}{d}\right)^{12} - \left(\frac{\sigma}{d}\right)^{6} \right] \tag{4.1}$$

where d is the interatomic separation between the outermost atoms of the tip apex and the surface, ϵ is the depth of the interaction potential well, and σ is a finite distance between the two atoms at which the potential is zero. The two terms ($\propto d^{-6}$ and $\propto d^{-12}$) distinguish between attractive and repulsive forces, respectively. The $\propto d^{-12}$ term arises from short-range repulsive chemical forces due to the Pauli exclusion principle and acting within a fraction of a nm. The $\propto d^{-6}$ arises from a contribution of long range (up to 100 nm) van der Waals types. In addition, there can be a variety of other forces, such as electrostatic (repulsive or attractive), electrodynamic (change in capacity), and adhesion forces (associated with meniscus formation). These can be rather strong, some of them will be described later as they are used as an imaging signal, but are neglected here. Thus, forces induced by the Lennard-Jones potential between a tip/sample are given by:

$$F(d) = -\frac{\partial U(d)}{\partial d} \tag{4.2}$$

Figure 4.1 shows a typical tip-sample interaction approximated by *U(d)*. When the tip and the sample are brought to close proximity, (d approaches zero), the interaction force causes the deflection of the cantilever, which is monitored and used for image formation.

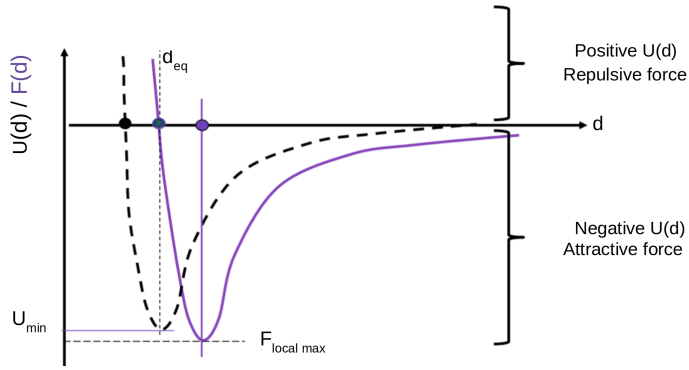

Figure 4.1: Interaction potential and force as a function of interatomic separation. Here d_{eq} is the separation at which the potential is minimum and the force is zero.

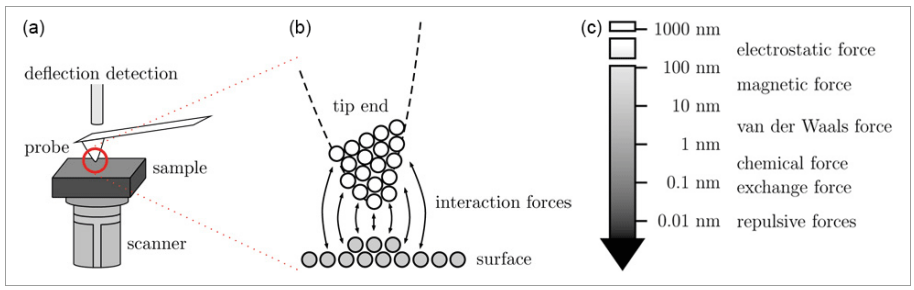

Figure 4.2: Schematics of the AFM setup (a) with a zoomed in view of the tip-sample interaction (b) along with the relevant forces and their ranges (c), from [57].

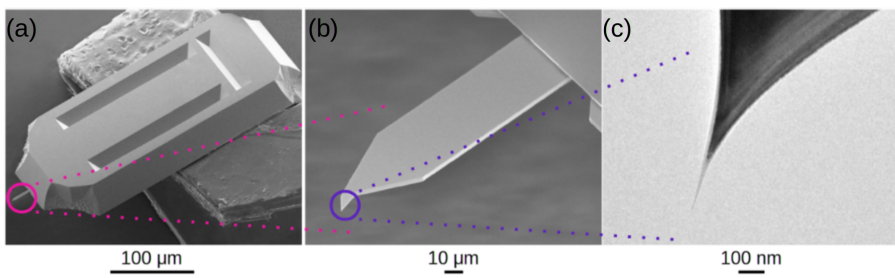

Figure 4.3: SEM images of (a) a typical AFM chip carrying (b) a cantilever with (c) a sharp probe tip at its end, adapted from [58].

A typical AFM spring-like cantilever is mounted onto a macroscopic holder, as shown in Fig. 4.3(a). The tip is situated at the free end of the cantilever (b) with the radius of the apex (c) of few tens of nanometers or even less. The cantilever acts a transducer - its role is to convert the forces that the apex feel during raster scanning into a deflection that can be measured. The choice of the cantilever material and dimension ultimately defines

the spring and its resonance frequency. Commercially available cantilevers are typically rectangular or v-shaped. Knowing the geometry allows establishing important cantilever quantities: 1) the force constant (k), 2) resonance frequency (f_{res}) and 3) the quality factor (Q). The force constant ultimately provides transformation of the interaction forces into force measurements, f controls the time response of the system, and Q provides a measure of hydrodynamic damping of the cantilever with the ambient environment [59]. Note, the cantilever has many resonances, and each is characterized by unique k and Q. For the further discussion I will refer to the frequency of the lowest flexural mode (vibration occurring in the direction parallel to the z motion of the cantilever) as a resonance frequency of the cantilever.

A typical force-distance *f-d* curve is shown in Fig. 4.4. The *f-d* curve provides the means to study the evolution of tip-surface interaction as a function of distance between. As the tip initiates approach/retract cycle, more than 100 nm away from the surface, the interaction is initially zero, however, as the distance is reduced (50-100 nm) the attractive forces begin to dominate causing downward bending of the cantilever. At the sub-nm separation, the tip enters repulsive net forces regime and the tip-surface contact is formed. Further reduction of distance leads to a strong backward bending of the cantilever. During retract cycle, the attractive (repulsive) forces begin to dominate (weaken) the interaction until the tip is back at the zero force line at which tip experiences zero net forces. Two discontinuities are observed, first, during loading as the tip jumps to contact when $dF/dz > k$ and second, during unloading due to adhesion. Based on the AFM imaging mode, it is possible to operate in both, attractive and/or repulsive regime.

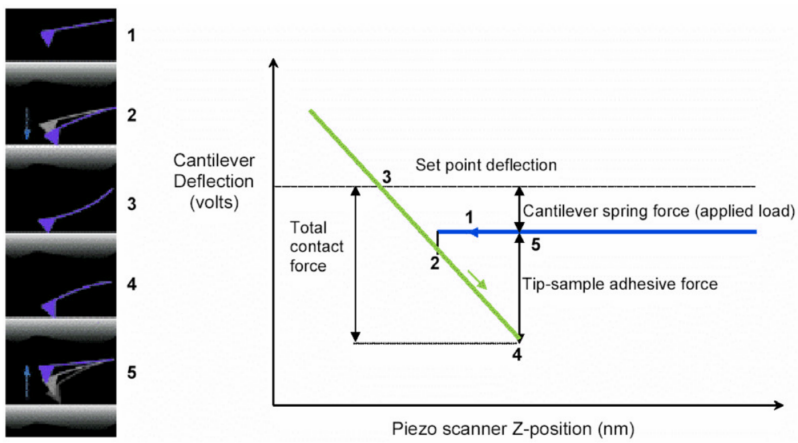

Figure 4.4: Typical force-distance curve showing different quantities that can be derived, adapted from [60].

4.1.2 Instrumentation

The main elements of AFM comprise an AFM head (the detection unit, cantilever system, and tip-surface motion system), a computer for processing signals, a power supply providing voltages to the piezoelectric actuators, and the sample stage, as shown in Fig. 4.5.

The AFM cantilever/tip assembly is fixed onto a block with its free part freely suspended. The block is attached to a piezoelectric scanner which generates relative motion (in x, y, and z direction) of the tip relative to the sample, see Fig. 4.5. The piezoelectric actuator (comprising the scanner) is usually a hollow segmented tube, allowing horizontal motions over large areas (typically $100x100\ \mu m^2$), while vertical motion is limited, on the order of 10-15 μm. During the scan, attractive or repulsive forces act on the tip causing the cantilever to bend. The cantilever deflection is monitored by a laser (or any light source provided it can be focused down to a point) beam directed towards the cantilever and reflected onto a photo sensitive detector. The photodetector consists of a four-fold segmented diode that provides a measure of vertical and lateral deflection.

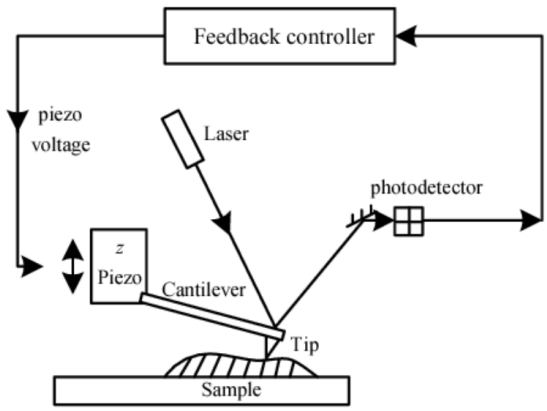

Figure 4.5: Scheme of the main elements of contact mode AFM. Piezoelectric element induces sinusoidal vibration of the cantilever at or slightly below its resonance and the vibration amplitude is measured by laser beam reflected on a detector. Either the sample stage or the AFM head can act as a scanner. The lateral directions of the scan are typically operated under open loop conditions, while the vertical (z) motion requires closed loop controller in order to record topography as a function of the set point, adapted from [59].

4.1.3 Imaging concepts

In the following section, three AFM imaging modes are discussed, based on the nature of the tip-surface interaction/deflection mechanism, 1) static mode (also called contact mode), 2) amplitude modulated mode [61] (known as tapping mode), and a relatively new member to the dynamic mode family 3) peak force tapping mode [62]. Note, frequency modulated [63] mode is kept out of discussion as it was not utilized during this thesis work.

Contact mode

Contact mode was the original AFM mode, which still has enormous significance being a fundamental basis of other scanning probe techniques, namely scanning capacitance- and conductive- AFM. The tip is continuously in contact with the surface, and the amount of repulsive force chosen by the user is termed setpoint. A feedback controller drives the z-piezo to keep difference between the set point and the actual deflection value (error signal) minimized. In addition to contact mode imaging, one can obtain *f-d* curves, which measures the forces directly while z-piezo motion is controlled using triangular signal.

At this point it is worth mentioning some drawbacks of this mode. Besides the inability to recover a part of the interaction force due to the discontinuities in the *f-d* curve, large friction is present capable of degrading the tip and the sample. For this reason there is a conflicting demand on the choice of the set point, high forces are required for stable contact and low enough to reduce the lateral interaction. To overcome this limitation dynamic modes have been developed.

Amplitude modulated mode

To preserve the tip and the sample, the amplitude modulated (AM) AFM mode [64] has been developed. In AM mode the cantilever is externally driven slightly below or at the resonance such that it oscillates above the surface. The oscillation is mainly driven acoustically, although different excitation mechanisms can be implemented (viz. magnetic, photothermal). During each oscillation cycle, the tip traverses through repulsive and attractive regimes, see Fig. 4.6.

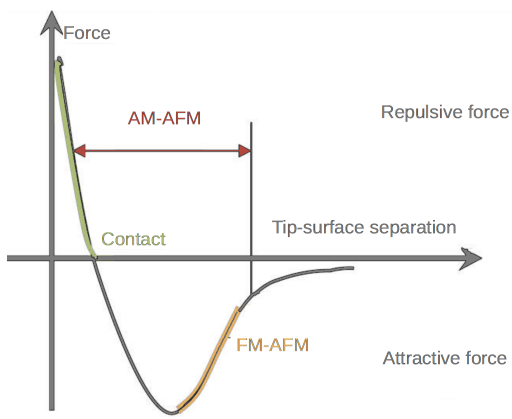

Figure 4.6: Imaging modes and their natures of tip-surface interaction.

If we drive the cantilever at its resonance, different forces will act on it resulting in a reduction in the amplitude of oscillation from its free value. However, if the cantilever is excited below the resonance, the oscillation amplitude can either increase or decrease. In the AM-mode, the observables are the amplitude and the phase lag that exists between mechanical excitation of the tip and the tip motion [59]. The root mean square (RMS) of the tip oscillation amplitude, as a result of interaction forces, is monitored by a controller which determines the error between the instantaneous oscillation and the reference value (setpoint) of the amplitude in order to maintain the setpoint characteristics of the cantilever oscillation. To ensure relatively constant forces between the tip and the sample the cantilever deflection error signal needs to be minimized. The amplitude of oscillation increases with the separation. The resolution of the AM-mode is dependent on the quality factor of the cantilever, which measures the energy loss of the oscillation [59].

Note, AM mode does not provide direct forces that the tip experiences during oscillation. During each oscillation cycle, the tip oscillates at or close to its resonance along the *f-d* curve and the attractive and repulsive forces dominate the response upon loading and unloading, respectively [62]. The force curve is not measured directly, the cantilever keeps oscillating and only the average values of forces are fed to the lock in. Forces and the transfer function of the cantilever are convoluted, the frequencies away from the resonance are filtered, and only average responses of all interactions are fed to the lock in amplifier. In addition, at cantilevers resonance the dynamics of the cantilever motion becomes rather complex. These are the weaknesses of the AM mode relative to the contact mode, where *f-d* curves record direct forces from which useful sample information can be gained. However, due to a very short tip-sample interaction, the lateral forces are reduced in AM mode, aiding to a better spatial resolution compared to the contact mode. Figure 4.7 shows an example of the same surface, consisting of flat InGaN islands separated by trenches, recorded with contact (left) and AM-AFM (right). Note that the sharp edges of the terraces and the depth of the trenches get much better reproduced in AM mode.

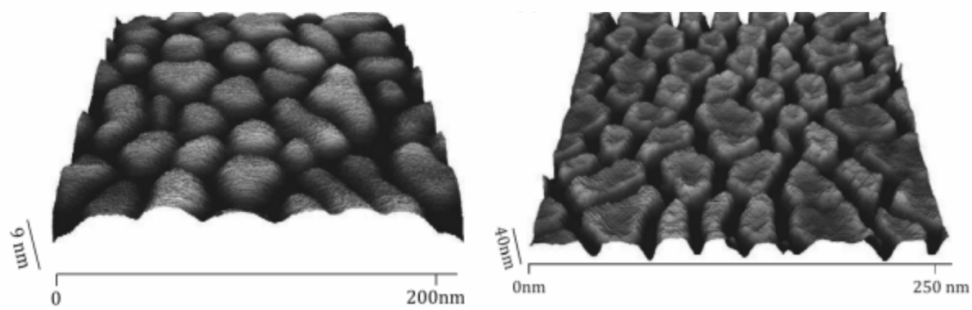

Figure 4.7: AFM image acquired on the same sample in contact mode (left) and AM mode (right).

The phase in the AM mode provides information about the material properties of the sample, namely surface composition and/or local energy dissipation variation. The phase shift is measured relative to the external excitation of the cantilever, as discussed in previous section. When the driving frequency is equal to the resonance frequency of the cantilever (undamped) the phase shift is 90° [59].

In Paper III, we have utilized the capabilities of the AM-mode to image InN QDs grown on GaN nanowires. In Fig. 4.7(a) a side facet of a NW is shown with a clear indication that the QDs (bright spots) nucleate at the edges between adjacent *m*-planes. QDs were found to preferentially nucleate at the edges, where they show lower residual strain than those nucleating on the *m*-plane. The phase shift (b) clearly shows a composition contrast between GaN nanowire side facets (blue) and InN QDs (yellow).

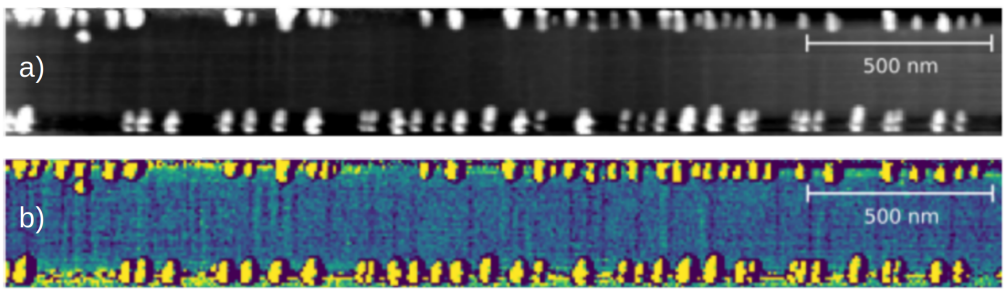

Figure 4.8: AM-AFM (a) topography and corresponding (b) phase image of a GaN NW *m*-plane highlighting QDs located at the plane edges.

Peak force tapping

At this point is should be clear that for long time after the development of the contact and AM-mode there has been a great desire to combine the strenghts and remove the flaws that both modes provide. Because of this, peak force tapping (PFT) has been invented. Similarly to contact mode, PFT measures direct forces, however, instead of triangular signal applied to acquire *f-d* curve, the z-piezo is controlled by a sine wave, reducing the resonances at the turnaround points [65]. And just like the AM mode, lateral forces are reduced by intermittently contacting the sample, but unlike it, it operates at off resonance mode. During the PFT operation, the cantilever is tuned way below its resonance (1-10 kHz) which means that the effects of the cantilevers dynamics that occur at higher frequencies will be reduced. The tip is controlled with a sine wave, such that the tip approaches the sample until the maximum repulsive force matches the setpoint. The feedback job is to keep this setpoint constant. Instead of measuring the average forces, a single interaction is reported, and this is the crucial aspect of PFT, the ability to remove parasitic deflections that decorate the tip-sample interaction [65] making the cantilever motion directly proportional to the

interaction force.

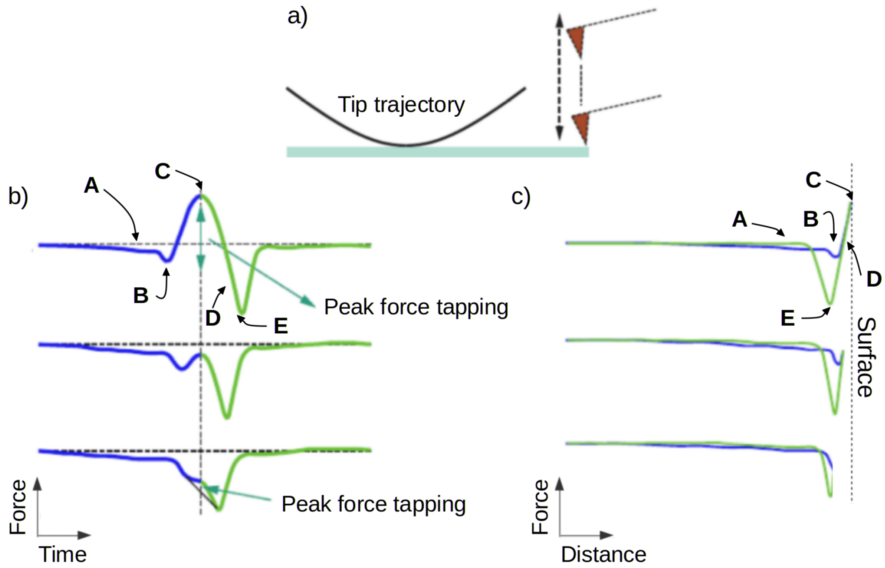

Figure 4.9: (a) Schematic tip movement during PFT. (b,c) Experimental force curve as a function of time (b) and distance (c) at modulation frequency of 2 kHz. Three different rows correspond to different setpoints (1 nN (top), -200 pN (middle) and -500 pN (bottom)), adapted from [60].

Experimental force curves as a function of time and Z at modulation frequency of 2 kHz are shown in Fig. 4.9. Three different rows correspond to different setpoints (1 nN (top), -200 pN (middle) and -500 pN (bottom)). Each curve shows approach (red) and withdraw (blue) of the cantilever. Figure 4.9(b) shows typical plot of the interaction force as a function of time in one modulated period (*f-t*), while Fig. 4.9(c) shows the corresponding *f-d* curve. The dashed vertical line on the *f-t* curve shows the maximum interaction force (the transition between approach and retract movement of *z*-piezo). The top row shows the standard configuration, with peak forces between 1 and 100 nN, as it was used in most cases of PFM performed in this thesis work. Of additional interest, however, is the information provided by the bottom two rows. Here, the peak force is detected although the setpoint is below the baseline (indicated by dotted horizontal line). This plot would be interpreted as a pure attractive force (below zero line) if feedback with averaged interaction (*e.g.*, AM mode) was used [65]. This operation allows scanning at much lower forces at which tip wear diminishes.

By measuring instantaneous forces and recording the force curve at each pixel during the scanning, the peak force mode enables separate evaluation of effects and sample properties such as adhesion, dissipation, modulus, and deformation, resulting in separate images which contain those properties [66]. For instance, Young's Modulus can be obtained by

fitting the slope of the segment C-D in the *f-d* curve using the Derjaguin-Muller-Toporov model [67] as shown in [66]

$$F - F_{\text{adh}} = \frac{4}{3} E^* \sqrt{R(d - d_0)^3} \tag{4.3}$$

where $F - F_{\text{adh}}$ is the force on the cantilever relative to adhesion, R is the radius of the tip apex, E^* is effective Young's Modulus, and $d - d_o$ corresponds to deformation of the sample. From this fit, provided Poisson's ratios of the tip (ν_{tip}) and the sample (ν_{sample}) are known, E^* is derived. Knowing E^* allows extraction of Young's Modulus through

$$E^* = \left[\frac{1 - \nu_{\text{sample}}^2}{E_{\text{sample}}} + \frac{1 - \nu_{\text{tip}}^2}{E_{\text{tip}}} \right]^{-1} \tag{4.4}$$

Furthermore, from the A-B segment during the approach curve (red) [66], one can extract the Van der Waals forces [68]. It is also possible to derive capillary adhesion (segment D-E) which greatly affects the tip during the retrace motion. For more on this topic a curios reader is referred to [62].

4.1.4 Calibration

To obtain reliable imaging, it is necessary to regularly calibrate x-, y-, and z- piezo scanners. Furthermore, all values that an AFM records are in volts, hence, in order to obtain quantitative force measurements and material properties, cantilever deflection (recorded in volts as the difference signal of the photodetector segments) as a function of piezo displacement needs to be converted to force units [59]. The following section is meant to provide the reader with four calibration steps required for any AFM measurements: 1) force constant, 2) the sensitivity of the optical system, 3) x- , y- and 4) z- calibration.

Cantilever force constant

In order to measure tip-surface interaction forces, the cantilever's force constant must be determined. The force constant (k) of a rectangular cantilever can be expressed as:

$$k = \frac{Ewt^3}{4L^3} \tag{4.5}$$

where E is Young's modulus and L, w, and t are the length, width and thickness of the cantilever. From here it becomes apparent that the force constant is highly sensitive to thickness which may vary throughout the cantilever length especially in the case of coated cantilevers.

This problem has been solved by different calibration methods [59], most notable the Sader [69, 70, 71] and the thermal noise [72, 73] method. During this work, k is calibrated by the thermal noise method which is based on equipartition theorem stating that in thermal equilibrium the average value of each quadratic term in the Hamiltonian is given by $k_B T/2$ [59]. For a free cantilever at equilibrium it follows:

$$\frac{1}{2}k\langle z^2\rangle = \frac{1}{2}k_b T \tag{4.6}$$

where $\langle z^2\rangle$ is the mean square deflection of the cantilever caused by the thermal fluctuations of the cantilever- a fundamental source of noise in AFM. In order to determine exact $\langle z^2\rangle$ (since the cantilever deflection includes distribution from all eigenmodes), the power spectral density over all frequency is measured [59].

Sensitivity of the optical system

In order to get meaningful units (length) for cantilever deflection and amplitudes, the output of the photodiode given in voltage has to be converted. Here a common volt-to-unit length conversion method is explained. First, the sensitivity in contact mode is determined by performing a typical *f-d* curve. This is performed on a hard surface, typically sapphire, where one can assume that basically no indentation of the sample occurs, but the scanner displacement in z direction is directly transferred into cantilever deflection. In order to calibrate detector signal (ΔV) with a known cantilever deflection, a line is fitted through the contact portion of the *f-d* curve (as explained earlier) leading to:

$$\sigma = \frac{\Delta V}{\Delta z} \tag{4.7}$$

where δz is piezo scanner displacement in the z direction. Care has to be taken here, because contact sensitivity (σ) is highly dependent on the laser alignment and the cantilever geometry, mainly the position of the laser spot and the cantilever length [59].

Piezo calibration

The AFM comes in open- and closed-loop piezo stages. Closed-loop indicates the presence of a sensor that monitors the piezo movement in nm units, and they do not require calibration. On the other hand, open-loop stages are prone to distortion in lateral (x and y) and vertical (z) piezos over time due to non-linear voltage-movement relationship of piezoelectric elements. To calibrate piezos, commercially available standard calibration gratings are used. The scanning is performed in contact mode and recorded in volts (supplied to x, y and z piezos). Knowing the dimensions of the gratings, it is then possible to calibrate

the measured dimensions (say in mV) to certain dimension of the grating along the x, y, and z direction. The conversion factor can be found in any AFM software. The procedure should be performed periodically, as piezos are known to change with time.

4.1.5 Atomic-scale topography imaging

Vertical and lateral resolution of a system are particularly important parameters. Vertical resolution can be defined as a minimum controllable height change and it is dominated by the noise in the imaging signal. The noise can be reduced by implementing probes with higher force constants and cantilever oscillation at resonance frequency. One way to define lateral resolution d, given by Bustamante *et.al.* [74], is

$$d = \sqrt{2R}(\sqrt{\Delta z} + \sqrt{\Delta z + \Delta h}) \tag{4.8}$$

where d, R, δz, and δh are shown in Fig. 4.10 for clarity. Here, it is assumed that the tip is parabolic and the imaged objects are infinitely sharp spikes such that when scanned over, the resulting image is a mirror of the tip shape. A small dimple (δz) is defined by the intersection of the two resulting inverted tip surfaces. The dimple is determined by the geometry of the tip and the separation d. From here, the lateral resolution is defined by the minimum separation d for which δz is larger than the noise of the instrument [74]. However, part (b) of the image complicates this situation further. Namely, by increasing the height of one spike δz decreases and one of the spikes fails to be resolved.

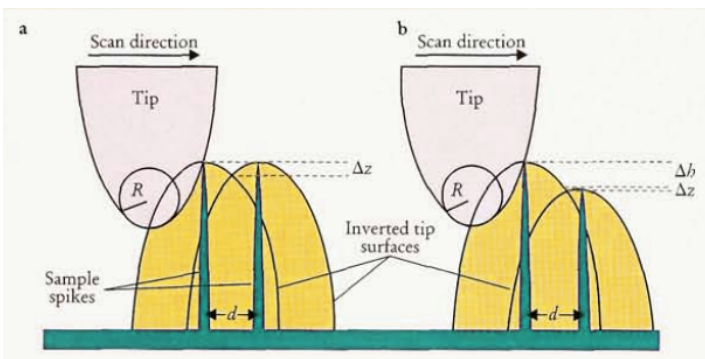

Figure 4.10: Resolution in AFM, from [74].

To improve lateral resolution both the noise and radius of tip's apex should be smaller than the periodicity of the features under investigation. In addition, using ultra sharp tips with high aspect ratio and minimum loading forces will lead to reduction of adhesion and will ultimately result in higher resolution images.

In Paper IV, AFM was utilized to study surface topography and step formation on InGaN platelets. Figure 4.11(a) shows a *c*-plane of a platelet (indicated in an inset) where surface steps are clearly resolved, corresponding to an atomic bilayer, which is the smallest possible step on GaN surface, with a theoretical height of 0.26 nm. By fitting steps, a step height of 0.30 ± 0.05 nm is obtained for In content corresponding to 9 %, reflecting the larger lattice parameter with increasing In content. For an In content of 18 % (not shown here), a step height of 0.32 ± 0.07 nm is measured. The noise level visible in (b) is smaller than a single step, on the order of 0.1 nm. A step appears to extend over 70 nm, with the limit of lateral resolution indicated by the slope in the staircase profile.

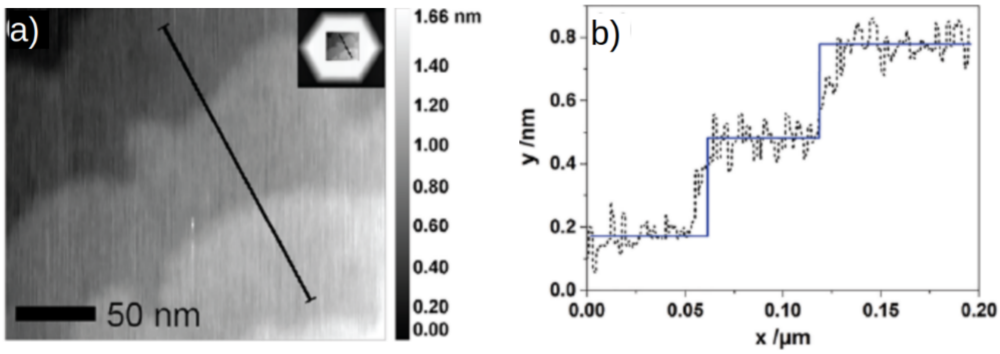

Figure 4.11: AFM images of the *c*-plane of InGaN platelets with indium contents of 9 % (a). Single bilayer steps were observed. Corresponding height profiles (as indicated by black lines) are presented in (b), from Paper III.

4.2 Conductive atomic force microscopy

Conductive AFM is commonly used to visualize local surface conductivity (current maps), where also local I-V curves can be obtained. However, in this thesis it was also used for modifying a surface by anodic oxidation, which will be introduced in the second part of the chapter.

4.2.1 Local currents

Imaging mode

Conductive AFM (c-AFM) is an indispensable current sensing technique for electrical characterization. Unlike the STM, the c-AFM provides the ability to record simultaneously real height and current map images, as shown in Fig. 4.13, as well as image conductive structures within insulating regions, where STM falls short.

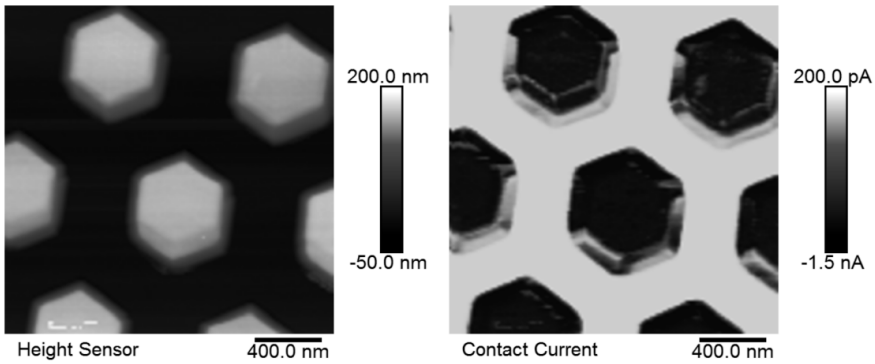

Figure 4.12: Simultaneously acquired topography (left) and the current map (right) of GaN platelets. The image is recorded at -10 V sample bias.

A constant DC bias voltage is applied to the sample and the measured current I is

$$I = A_{\text{eff}} J \tag{4.9}$$

where A_{eff} is effective tip-sample contact area and J is the current density. Note, J depends on the applied DC bias, conductivity of the tip and the sample, and local inhomogeneities in the sample (e.g., defects). A_{eff} is affected by the choice of the set force, the force constant of the tip/sample system, and the relative humidity. Note, A_{eff} carries an information of all electrical effects that may arise within the tip-sample contact. Even if current densities are large, the typically very small value of A_{eff} results in small measured current I. A good (state-of-the-art) c-AFM system has low enough noise to enable to extract currents in the femto-ampere range.

In contact mode, set forces are sample/tip dependent, a small force will yield to less damage on soft samples but also unstable contact and unreliable current measurements, whereas higher forces lead to a larger contact which then improves the current sensitivity and helps enabling a good contact even in the presence of a thin oxide layer or other contaminants on the sample surface. A problem arises because forces required for imaging are much lower than the forces required for current detection. In order to increase the life time of the probes dynamic mode is preferred. However, the standard AM-AFM here does not work because the tip-sample contact time is very short, less than 0.1 μs, prohibiting effective current detection.

For this reason it is favorable to use PFT mode. Three different current signals can be extracted: 1) peak current, 2) average (also called Tuna) current, and 3) contact current. Peak current is an instantaneous current at point C, according to Fig. 4.13, when the tip peak force is detected. This can also be the maximum current, but it is not necessarily so, as due to the limited rise time imposed by the bandwidth of the module or the resistance-capacitance of the sample there may be a lag in the current response [**?**]. Tuna current

is the average current through one tip oscillation cycle, point A-E, recorded while the tip traverses through attractive and repulsive regime. Contact current, finally, is the average current while the tip is in repulsive regime (from B to D).

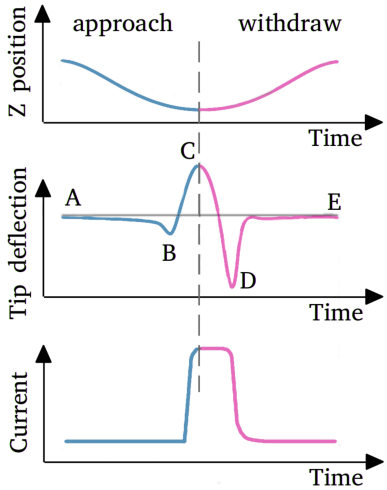

Figure 4.13: Schematics of a single Peak Force Tapping cycle: Z position, force, and current as a function of time. A and E are the points where the net forces are zero, B indicates jump to contact, C peak force, and D is the adhesion point, from [?].

Tip-sample Schottky barrier

During this thesis work conductive measurements have been recorded on semiconductor samples, where the measured current strongly affected by a Schottky barrier formed between the tip and the sample. Figure 4.14(a), shows the metal (tip) and *n*-type semiconductor (sample) separated at some distance. Upon contact, the Schottky barrier is formed when the work function of the metal exceeds that of the semiconductor, since the vacuum level has to be continuous. The resulting energy band diagram is shown in (b), for an *n*-type semiconductor-metal contact under zero bias condition.

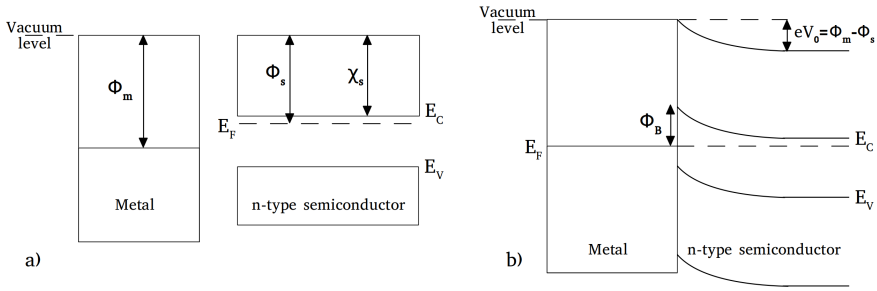

Figure 4.14: Metal *n*-type semiconductor contact. a) The metal and semiconductor not in contact, b) Schottky barrier formation under zero bias. For simplicity, no surface states are assumed at the semiconductor side.

Just like in an *n*-type side of a *p-n* junction, due to the positive charge on the ionized donors, the bands are bent upwards establishing a barrier for electrons. The height of the barrier seen from the metal side ϕ_B is

$$\phi_{\mathrm{B}} = \phi_{\mathrm{m}} - \chi_{\mathrm{s}} \tag{4.10}$$

where ϕ_{m} and χ_{s} are the metal work function and semiconductor electron affinity [75]. However, experimentally ϕ_{B} is found to be less dependent on the choice of the metal, due to the effect of surface states [76] which arise because the surface terminates the periodicity of the matrix crystal [77]. In most practical contacts, the semiconductor surface states, characterized by a neutral level ϕ_{o} (level to which the surface states are filled when the surface is electrically neutral), are present. If the neutral level sits above the Fermi level, the surface states will contain a positive net charge leading to the reduction of depletion region and hence decrease band bending, resulting in a decreased Schottky barrier height. The reduction of ϕ_{B} has the effect of pushing the neutral level towards the Fermi level. For the case when the neutral level is located below the Fermi level, the net surface charge is negative, leading to the increase of the depletion region and bend bending as the neutral level is pushed towards the Fermi level. This modifies Eq. 4.10 to

$$\phi_{\mathrm{B}} \approx E_{\mathrm{g}} - \phi_{\mathrm{o}} \tag{4.11}$$

where the barrier height is said to be "pinned" by the high density of surface states [78].

For an ideal Schottky contact, given the metal work function exceeds that of semiconductor, the rectifying behavior is expected. Forward biasing the junction, decreases the band bending and the size of the depletion region, and the electrons begin to flow. Contrarily, reverse biasing the contact would increase the barrier and the electron flow would be limited. For an ideal Schottky diode, current under reverse bias condition should saturate at the value

$$I_{\mathrm{o}} = AA^{**}T^2 \exp\frac{-q\phi_{\mathrm{B}}}{k_{\mathrm{B}}T} \tag{4.12}$$

according to the thermionic-emission theory [78], where A is the area of the Schottky contact, A^* is the Richardson constant, T is the temperature and k_B is the Boltzmann constant. However, as it will become apparent in the following section, the current may not saturate, but rise following the exp term in Eq. 4.10, due to image force lowering, presence of an interfacial layer, tunneling through the barrier, generation of electron-hole pairs in depletion region, etc. [78].

I-V spectroscopy

In addition to imaging modes, local current-voltage (I-V) spectra can be obtained at the local point of interest by interrupting the scan movement of the tip and varying the applied bias while measuring the resulting current. Here I examined the I-V characteristics of n-type GaN nanowires, as shown in Fig. 4.15, where left hand side plot shows the forward bias characteristics (corresponding to negative sample bias), of a seemingly stable contact, whereas the right hand side of the image shows current instabilities during the measurements. Furthermore, the current is sensitive to the tip-contact area, and therefore to the tip-loading forces.

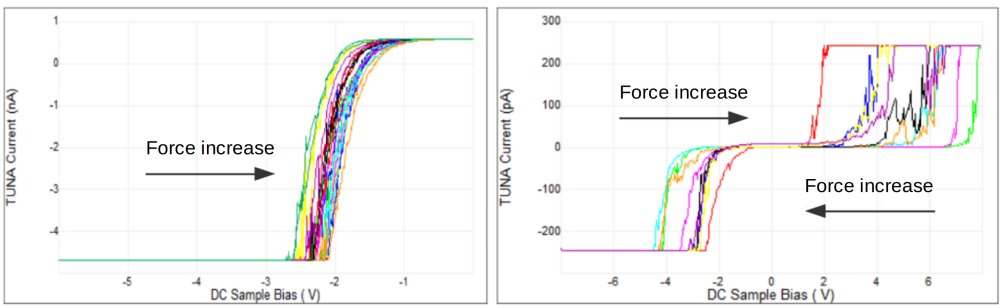

Figure 4.15: Influence of the loading force on I-V characteristic. The I-V curves are recorded at different tip loading forces 3-40 nN, at two different locations for curves shown in left and right hand side plots. Note, the forward bias direction is plotted over negative voltage, since the AFM setup utilizes sample biasing, and the tip is considered grounded.)

Although beyond the scope of this thesis, it is possible to extract the Schottky barrier height from the I-V curves, if the Richardson constant and the tip-surface contact area are known, since the saturation current I_o from a linear fit of a semi-log I-V in the forward bias region is obtained from the recorded I-V curve, through Eq. 2.20.

4.3 Local anodic oxidation

A special application enabled by c-AFM, or an effect resulting from c-AFM imaging, is local anodic oxidation, which means local oxidation of the sample surface in the electric field of the AFM tip. This has been used since the 1980s for scanning probe lithography (SPL) as a promising tool capable of patterning a variety of conductive and insulating materials on a nanoscale [79]. Although both AFM and STM have been used, the STM has significant problems if the oxide gets thicker as it requires a conductive surface, otherwise resulting in instabilities in tunneling current and even tip crash.

The first report of oxidation-SPL dates back to late '80s [80]. Today, the method has made a huge impact where e.g. sophisticated quantum devices [81, 82] and field effect transistors [83, 84] have been created with sub-nanometer resolution [85].

4.3.1 Principles

Oxidation-SPL allows local modification of the material through anodic oxidation assisted by strong electrical fields (10^8 - 10^9 Vm^{-1}) arising at the probe-sample interface. When operating in ambient environment with humidity over 20 %, the capillary condensation leads to formation of a water meniscus, see Fig. 4.16(b). When the surface and the probe are brought to close proximity, the water bridge forms at the tip/surface interface. By application of positive sample bias, a strong electric field develops between the very sharp tip and the surface. This field breaks the water molecule, driving the negative ions (anions) towards the surface (biased as anode), where they recombine to form an oxide, hence the name anodic oxidation. This technique is applicable to both static and dynamic AFM.

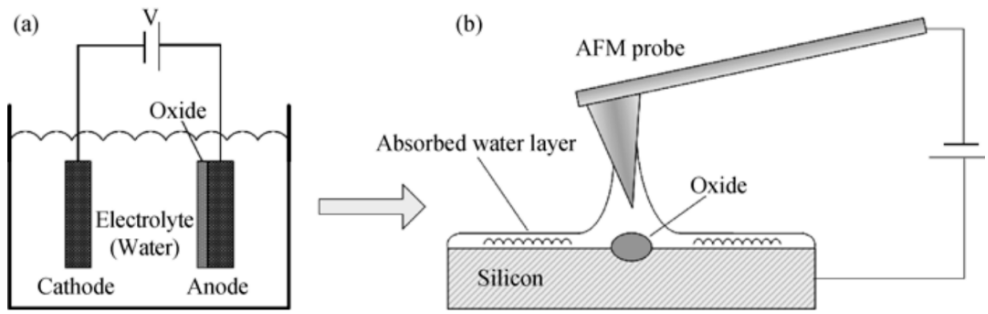

Figure 4.16: Schematics of local anodic oxidation comparing (a) a traditional electrolytic cell, and (b) a micro electrolytic cell with a c-AFM probe used as cathode, from [86].

4.3.2 Anodic oxidation of GaN

In Paper II, I use anodic oxidation not for writing structures on a homogeneously conductive surface as in SPL, but instead for visualizing and passivating conductive channels in a heterogeneous sample, see Fig. 4.17. The sample consists of coalesced nanowires (their location is highlighted with orange hexagons in (a)) that have formed a continuous thin film. The image shows the height gradient, created by emphasizing the edges and surface steps using the lateral derivative of the height signal. The same area is scanned again under 10 V sample bias and at a relative humidity of 30 % resulting in the shown current map (b) and corresponding topography (c). Comparing Fig. 4.17(c) to part (a) and (b), it becomes apparent that the topographic changes occurred over nanowire cores and dislocations in the coalesced matrix. Note, a positive bias applied to the sample and its *n*-type NW cores results in a reverse biased tip-sample Schottky barrier. Therefore, the current observed here is a leakage current, induced by electrically active defects in the GaN. The leakage current has been attributed to deep level point defects, such as Ga vacancies and carbon, both expected in *n*-type GaN. These deep level defects are known to create localized levels within the band gap and act as charge carrier traps, causing degradation of devices. It is recognized that defect-assisted tunneling mechanisms in GaN Schottky interfaces lead to an increase in leakage current.

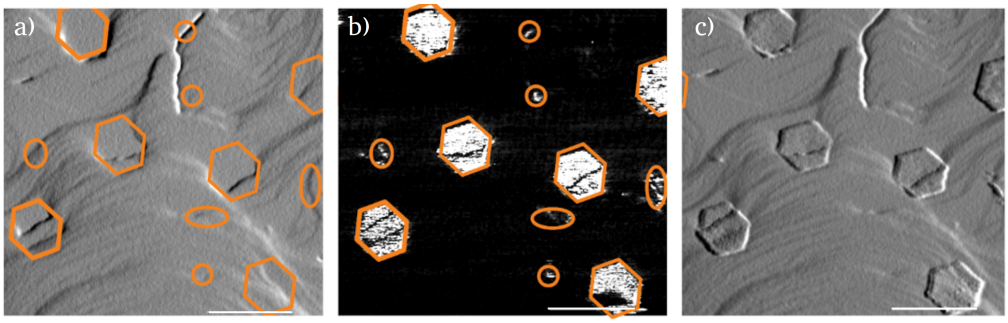

Figure 4.17: AFM gradient of topography image before local anodic oxidation of a GaN nanowire film formed by reformation. Hexagons indicate the location of the NW cores. Simultaneously acquired (b) current map and (c) topography of the same area during local anodic oxidation at 10 V sample bias and 30 % relative humidity. The oxide formed on the conductive hexagonal cores (b) and increased their height (c), revealing their position and shape much clearer than in (a). The scale bar indicates 500 nm.

4.4 Kelvin probe microscopy

In 1991 Nonnenmacher [55] modified the AFM to measure a contact potential difference (CPD) between the surface of the sample and the tip. Contrary to the Kelvin method where a current is monitored, the KPM takes advantage of the electrostatic forces, allowing measurements of insulators [55]. Besides probing material work function, it is capable of

measuring doping levels of semiconductor, active defects, etc.

4.4.1 Operating principle

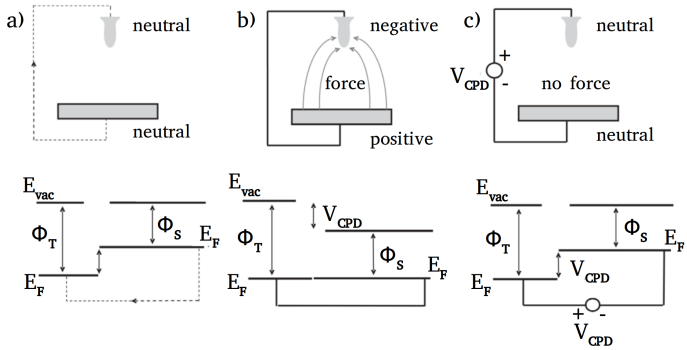

Figure 4.18: Illustration of Kelvin probe measurement setup. Energy levels of the tip and surface are shown for three cases: (a) tip-surface separated by some distance with no electrical current, (b) tip-surface in contact, and (c) under external bias (V_{tip}) applied to nullify the CPD, adapted from [87]

Figure 4.18 shows a simplified schematic of the tip-surface band diagram with work functions of the tip ϕ_T and of the sample ϕ_S. When a tip and a sample are separated by some distance (a), their vacuum levels are the aligned and the tip and the sample surfaces are neutral. Establishing external contact between the tip and the sample (b), the Fermi levels will align through current flow from a material of a lower work function (here ϕ_S) to a material of higher (ϕ_T) resulting in a charge formation at the tip/surface interface. Due to the charging an electrostatic force develops and an apparent contact potential difference V_{CPD} which equals the offset in tip-sample vacuum levels. V_{CPD} is then defined as:

$$V_{CPD} = \frac{\phi_T - \phi_S}{e} \tag{4.13}$$

where e is elementary charge. The idea of KPM is to measure this electrostatic force, compensating the charge by applying an external bias V_T to the tip, and finding the condition $V_T = V_{CPD}$, resulting in zero charge and force, while scanning the sample, thus mapping the local CPD. The electrostatic force between the AFM tip and the sample is given by:

$$F_{es} = -\frac{1}{2}\left[\Delta V\right]^2 \frac{dC(z)}{dz} \tag{4.14}$$

where $\Delta V = V_T - V_S = V_T \pm V_{CPD}$ and $dC(z)/dz$ is the gradient of the capacitance between the tip and the sample surface. The bias applied to the tip has both DC (V_{DC}) and AC (V_{AC}) component, the latter generating an oscillating electric force and ΔV becomes:

$$\Delta V = V_T \pm V_{CPD} = V_{DC} \pm V_{CPD} + V_{AC} sin(\omega t) \tag{4.15}$$

The expression of the electrostatic force applied to the AFM tip is derived substituting Eq. 4.14 in Eq. 4.15:

$$F(z,t) = -\frac{1}{2}\frac{dC(z)}{dz}[V_{\mathrm{DC}} \pm V_{\mathrm{CPD}} + V_{\mathrm{AC}} sin(\omega t)]^2 \tag{4.16}$$

This equation can be separated into three components:

$$F(\mathrm{DC}) = -\frac{dC(z)}{dz}[\frac{1}{2}(V_{\mathrm{DC}} \pm V_{\mathrm{CPD}})^2] \tag{4.17}$$

$$F(\omega) = -\frac{dC(z)}{dz}(V_{\mathrm{DC}} \pm V_{\mathrm{CPD}}) V_{AC} sin(\omega t) \tag{4.18}$$

$$F(2\omega) = \frac{dC(z)}{dz}\frac{1}{4}V_{\mathrm{AC}}^2[cos(2\omega t) - 1] \tag{4.19}$$

where ω is the modulation frequency of the AC bias and t is time. The DC part of F(DC) measures the topographic signal, $F(\omega)$ contribution is used to measure the contact potential difference, and the $F(2\omega)$ part can be used for capacitance microscopy. Amplitude-modulated (AM)-KFM measures $F(\omega)$ from the amplitude of the cantilever oscillating at ω induced by V_{AC}, while V_{DC} is varied such as to nullify the measured amplitude by compensating V_{CPD} and the correspondingly found $V_{\mathrm{DC}}(F(\omega) = 0)$ equals V_{CPD}. If the tip workfunction Φ_{T} is known, the local work function of the sample surface Φ_{S} can be calculated by Eq. 4.13.

4.4.2 Detection of V_{CPD}

The AM-KPM imaging scheme during this thesis work operates under lift mode: The trace of each scan line is recorded under regular AM mode, resulting in topography measurements. During retrace scan direction, the tapping movement of the z piezo and the imaging feedback are interrupted, the tip is lifted up by about 50 - 100 nm, in order to leave the influence of short range forces, and scanned back across the sample following the same height trajectory of trace. Here, the cantilever oscillation is driven by application of V_{AC} at the resonance in order to enhance the signal and reduce further short range forces. The amplitude of oscillation depends both on the DC bias and the surface potential of the sample. DC bias is applied between the tip and the sample until the electric field vanishes, at which point the oscillation stops and the DC voltage then provides the potential of the sample.

Note, the recorded signal provides a measure of the voltage required to compensate long distance electrostatic forces at each pixel of a scanned electric field distribution. The signal is then convoluted between electrostatic interaction of the the entire tip cone and cantilever with the sample. This is a limiter on the accuracy and lateral resolution of the measurement

performed with KPM. Furthermore, the measured signal is dependent on the tip lift height, with higher lift heights being desirable, however, hurting the spatial resolution that decays with the tip-surface separation.

4.4.3 Detection of local polarity inversion at GaN surfaces

In Paper I we have investigated the surface polarity of GaN with KPM, see Fig. 4.19. No correlation has been found between topography (left) and the potential map (right). The topography image shows well defined steps and terraces while the position of the coalesced NW cores is not obvious. The KPM image shows a two-fold distribution of the surface potential: low potential is measured over large areas with a clear boundary, sometimes following the contour of single NW cores, and rather homogeneous potential, which is about 100-150 mV below the potential outside. This boundary has been associated (and later confirmed by etching under NaOH) to inversion domain boundaries, where the lower potential is associated with areas with an N-polar surface, embedded in a GaN crystal with Ga-polar surface.

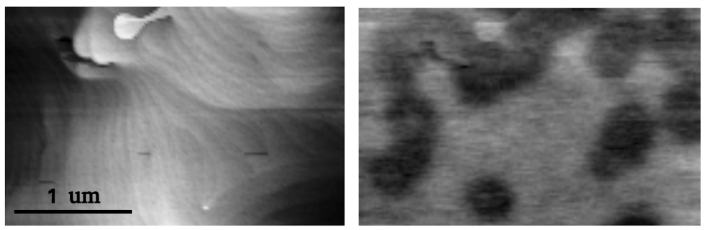

Figure 4.19: AFM topography (a) and corresponding KPM (b) image of a GaN film formed through reformation. Darker spots in the KPM image have been attributed to N-polar domains in an otherwise Ga-polar crystal matrix.

4.4.4 KPM on nanowires

As we have seen earlier, one of the major artefacts in the topography signal is the effect of broadening- the convolution of the imaging tip shape and the object under investigation. The effect is pronounced further as topography height increases, placing a strong limiter on the KPM, where electrostatic force of the tip cone and the cantilever play a stronger role. A signal detected over features with large height difference would result in a weighted average of the work function of the nanowire and the substrate. As the tip shifts toward and away from the edges of the nanowire, the cantilever proximity to the surface changes, giving a rise to the slope in the potential, due to the capacitive coupling of the tip cone and the cantilever. The effect is pronounced further if protrusions on the AFM probes exist, due to breakage, contamination, etc. Such protrusions are infamous for the observed

double/multiple tip effect. Furthermore, electric field lines dominate the edges, making data interpretation difficult.

In Paper VI, KPM is utilized to map the potential along 2.5 μm long and 200 nm wide NWs containing an axial pn-junction, as shown in Fig. 4.20(a). The corresponding lines A and B are plotted as a function of height in (b). The height profile shows a flat NW sidewalls, with around 10 nm surface corrugation. Figure 4.20(c) shows a map of the surface potential, with two distinct regions, *n*-type (indicated green) and *p*-type (purple). The relatively small potential difference between the two segments, as compared to the open-circuit voltage of 0.7 - 0.8 V measured for similar InP NWs [88] has been attributed to the native oxide, existing surface states, and defects, resulting in surface band-bending.

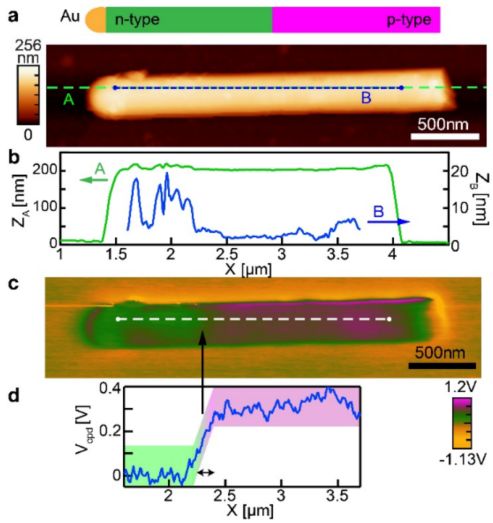

Figure 4.20: Potential distribution along the p-n InP NW. (a) AFM image of NW topography, with lines A and B plotted as height profiles in (b). (c) KPM image of the same area, highligthing the contrast in potential over *p*- and *n*-doped segments of the NW. The contact potential difference along the indicated line is plotted in (d).

An interesting example that highlights the sensitivity of KPM to surface preparation is shown in Fig. 4.21. InP nanowires, transferred onto a foreign substrate, have undergone surface oxide is removal in hydrogen environment at $2x10^{-6}$ mbar and 400° C. Figure 4.21 shows (a) AFM topography and (b) surface potential of an InP NW after oxide removal. The NW has undergone a $-45°$ rotation (original NW location is indicated by dashed green rectangular) during AFM scanning, being pushed by the AFM tip. The topography image shows the height variation along the NW at its final position, with no indication of the original NW location, whilst KPM image shows a similar level of potential at the original NW location as to the NW surface. This indicates that some small amount of InP has been deposited on the substrate underneath and around the nanowire during the cleaning procedure, which remained while the nanowire itself was pushed away by the AFM

tip.

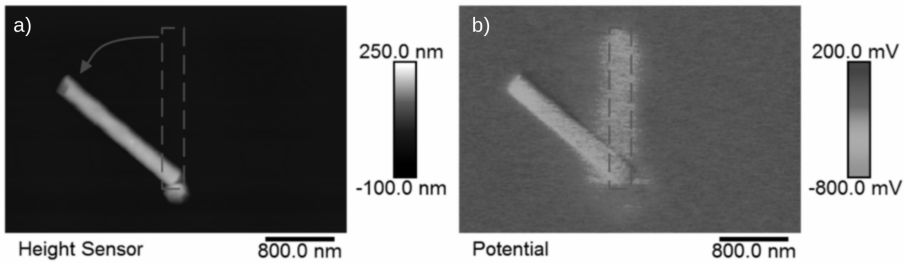

Figure 4.21: AFM (a) topography and (b) surface potential of an InP NW after annealing. The NW has undergone -45° rotation during the scan. The original NW location is indicated by a green rectangular. The substrate at the previous NW location shows a similar potential as the NW surface, highlighting the impact of surface modification and sensitivity of the KPM.

4.5 Scanning Capacitance Microscopy

SCM [56] utilizes local interaction between a metallic tip and a semiconductor sample allowing mapping of dopant type and distribution in a semiconductor device on a nanometer scale. It is a modified AFM in which a conducive probe measures a differential capacitance dC/dV of a metal (tip) - oxide- semiconductor (sample) (MOS) junction simultaneously with topography. The native oxide can be sufficient to electrically insulate the sample from the tip, otherwise a thin high-k oxide can be deposited. A low frequency AC signal is applied between the tip and the semiconductor surface in order to deplete and accumulate free carriers in the semiconductor near the surface, see Fig. 4.22. The applied AC field results in a varying capacitance that is detected by a high frequency capacitance sensor, capable of detecting $10^{-22}\mathrm{F/Hz}^{-1/2}$. The capacitance sensor produces the voltage proportional to the differential capacitance which is measured with a lock-in amplifier. The lock-in amplifier, referenced to the modulation frequency f_{mod} is used to measure the phase and the amplitude of the sensor output voltage. The phase channel provides the information of the carrier type, while amplitude corresponds to the carrier concentration as seen in Fig. 4.23.

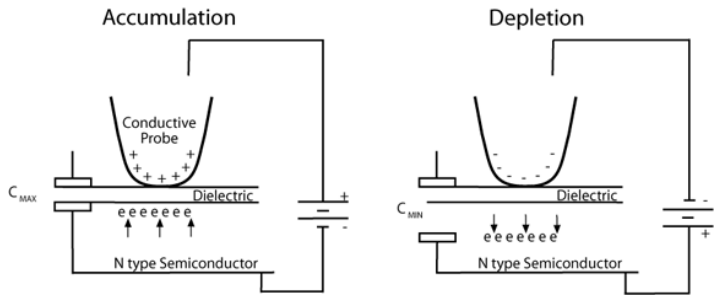

Figure 4.22: Schematics showing charge carriers accumulated and depleted under applied bias, from [60].

A typical capacitance- versus- voltage C-V curve for an n-type semiconductor is shown in Fig. 4.23. Higher (more positive) voltage at the tip results in accumulation of the sample and higher capacitance, while lower (more negative) voltage results in depletion and lower capacitance. High carrier concentration material depletes slower, so that the capacitance decreases less for the same decrease of voltage as compared to material with lower carrier concentration, resulting in a smaller dC/dV. Response of a p-type material is 180° out-of phase. An SCM amplitude image is constructed from the change in capacitance (dC) in response to the low frequency AC bias (dV) and represents the slope of the capacitance-voltage C-V curve at V_{DC}, and therewith the charge carrier concentration. The SCM phase can also be imaged, distinguishing between n-doped, p-doped, or intrinsic material. In addition to a V_{AC}, V_{DC} bias is applied, which modifies the operation point in the transition region of the dC/dV curve.

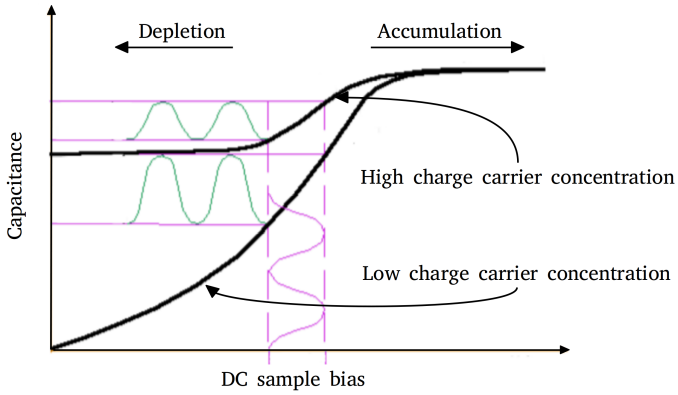

Figure 4.23: Typical capacitance- versus- voltage curve for an *n*-type semiconductor, modified from [89].

The spatially probed area is dependent on tip radius, oxide thickness, local dielectric constant, and voltage between the tip and the sample [90], and is, as a rule of thumb, comparable to the square of the tip radius. On the other hand, the vertical extension of the probed volume is a function of material properties of the sample, for example, for materials with relatively high concentrations of free charge carriers, as in doped semiconductors, the probing depth is much smaller than the tip radius [90].

The system consists of two capacitors in series, one from the oxide, the other from the active depletion region just below the oxide-semiconductor interface. This means that total capacitance is dependent on the quality of the oxide film, depletion region thickness, applied DC bias, carrier mobility which can be degraded near defects, etc.

Figure 4.24, taken from Paper I, shows (a) height information, (b) the *dC/dV* phase, and (c) the *dC/dV* amplitude corresponding to distribution of free charge carriers in a GaN film consisting of coalesced nanowires. The measurements reveal variations in the phase channel: NW cores and the coalesced matrix-material is *n*-type (bright signal) whereas the NW shells are *p*-type (dark). Non-intentionally doped GaN (0001) surfaces are often found to be *n*-type, explained by silicon and oxygen impurities, whereas *p*-type behavior is not expected. In the amplitude image (c), a higher signal (brighter contrast) corresponds to a lower charge carrier concentration, and vice versa. However, the amplitude signal is rather homogeneous with an in average ca 10 % lower signal (higher concentration) at the shells.

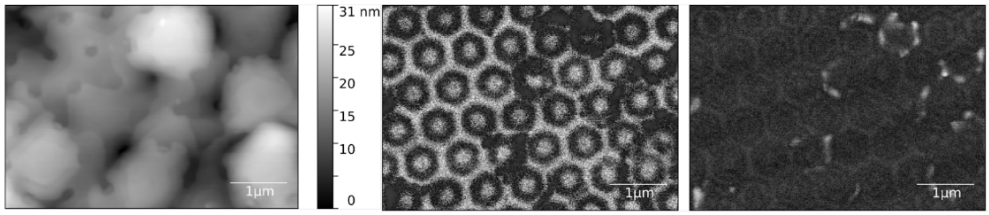

Figure 4.24: Simultaneously acquired AFM images showing (a) topography and (b) phase and (c) amplitude of the scanning capacitance microscopy *dC/dV* signal. The unintentionally doped sample consists of *n*-doped NW cores and coalesced matrix (bright) and *p*-doped shells (dark), which can be distinguished in (b). Brighter contrast in (c) corresponds to regions with lower charge carrier density and vice versa.

4.6 Scanning Tunneling Microscopy

Scanning tunneling microscopy is a technique based on quantum electron tunneling allowing simultaneous study of the structure and electronic density of states of conductive surfaces, providing atomic resolution. During this work, STM and scanning tunneling spectroscopy have been utilized to study *p*-*n* junction InP nanowires, explained in the following section. In addition to a regular use, we have also employed the STM in an unorthodox manner where the probe has been used to both image and contact (point contact) the upright standing nanowires allowing the study of opto-electrical properties, as described in Section 5.3.

4.6.1 Principle and setup

Figure 4.25 illustrates dependence on the electron tunneling on the direction of the bias and its magnitude. Applying a positive sample bias, see (a), electrons tunnel from filled metal states into empty conduction band states of the semiconductor. In the same fashion, when a negative sample voltage is applied, the electrons tunnel from filled states of the sample into empty states of the tip.

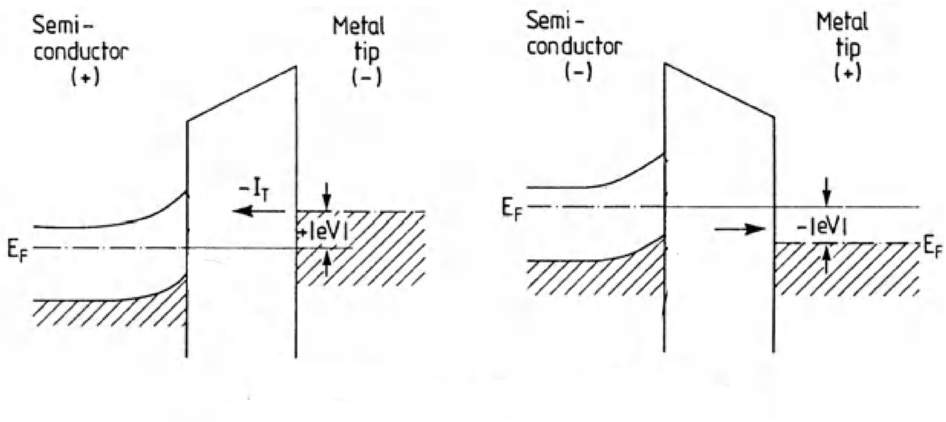

Figure 4.25: Schematic diagram of the STM tip and the semiconductor surface. (a) At positive sample bias, tunneling of electrons occur from the metal tip into empty states in the sample. (b) At negative sample bias, tunneling occurs from occupied surface in the sample into the metal, modified from [91].

As a first approximation, based on one-dimensional electron tunneling, the tunneling current I_T [92] can be expressed as:

$$I_T \propto \exp(-2\kappa d) \tag{4.20}$$

where, κ is the inverse electron decay rate and d is the width of the vacuum barrier (tip-sample separation). This exponential dependence of the tunneling current on the tip-sample distance is what enables sub- Å vertical resolution. The tunnel current, as the rule of thumb, changes by a factor of ten for every increase of the barrier width by 1 Å allowing its use as a height monitor.

Just like in the AFM, the piezoelectric element causes a raster movement of a sharp metallic tip over a conductive substrate. The measured current is amplified and converted to a voltage used as an input to a feedback loop. The feedback loop aids in adjustment of the tip position by comparing the measured current to a set value. This mode is implemented when scanning under constant current mode, which is usually the case. In order to keep the tip-sample separation within tunneling distance, the STM requires rigorous vibration control and operation under ultra-high vacuum conditions (UHV, pressure below 10^{-9} mbar). This is advantageous because the UHV environment is ideal for preparing atomically clean surfaces by electron- and ion-beam experimental techniques.

In order to scan the side walls of NWs, NWs are first broken off from their growth substrate and deposited on a suitable substrate. Native oxide is removed by annealing in atomic hydrogen [93, 94], resulting in atomically resolved images of the clean NW surface.

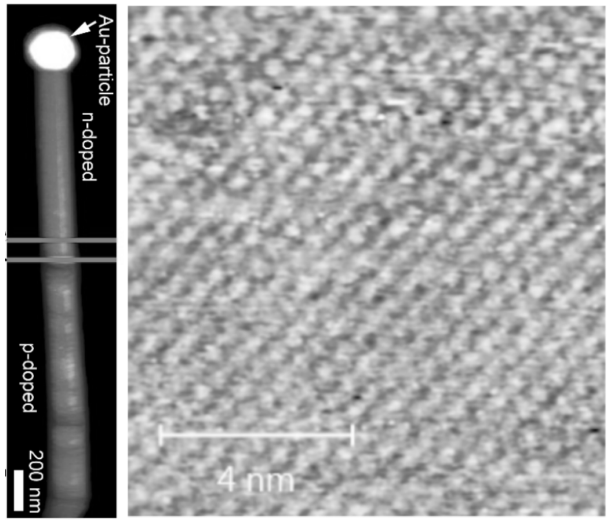

Figure 4.26: Atomically resolved STM image of an InGaP NW site facet, showing individual P atoms arranged on a 110 surface demonstrating successful surface oxide removal.

4.6.2 STM as nanoprobe for investigation of as grown InP nanowires

During this thesis (Paper VI), the STM has been also implemented in an unorthodox manner in order to both image and contact an individual nanowire, still standing upright on its original substrate, as shown in Fig. 4.27. First, the STM probe has been used to locate single nanowires by STM imaging, which was initiated by a traditional auto-approach. The tip and the nanowires are brought together until a tunneling current is detected, as indicated in (a). Because the tip may land either on top of nanowire or in between them, it is required to retract it some distance away (usually the length of the nanowire) allowing a safe scan over a large area. If no signal is detected at this stage, the tip is moved closer to the substrate and the scan is repeated. This procedure is repeated until the tip and the top end of the NWs are close enough to create an interaction for a feedback, resulting in an overview image like the one shown in Fig. 4.27(b).

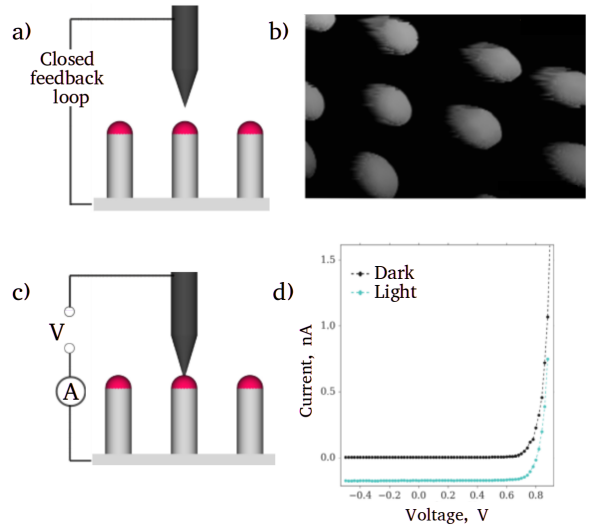

Figure 4.27: Experimental setup for imaging and contacting upright standing nanowires using STM. Imaging of nanowires with the STM electronics as sketched in (a), results in an STM image shown in (b). Here only top the {100} nm segment of the nanowire is imaged. Contacting involves 1) interruption of a feedback loop, 2) controlled pushing of the STM tip into the nanowire, and 3) an external preamplifier to record the $I-V$ curves, in light and dark, shown in (d).

Next, the reference image (obtained in the previous step) is used to place the probe in the NW center, which is typically at the largest z-piezo voltage, and the feedback is interrupted. The tip is then moved manually towards the sample aiding in the point contact formation. The current signal is fed to an external low-noise current amplifier and the *I-V* data is recorded, as shown in Fig. 4.27(c,d). Timm *et.al.* [95] have previously demonstrated realization of Ohmic contact formation between the W tip and the Au particle sitting at the top end of a NW.

In Paper VII, I investigated the photovoltaic behavior of InP *p-n* junction NWs. Figure 4.28 shows a linear and corresponding semi-log plot of a typical *I-V* curve, in dark (black curves). The ideality factor of 1.86 suggests that some recombination of carriers occurs in the quasi-neutral region. The photovoltaic performance was assessed by illuminating the sample, resulting in a shift of the *I-V* curve (red curves). I obtained an $I_{SC} = 0.14 \pm 0.03$ nA, an open-circuit voltage of $V_{OC} = 0.75 \pm 0.02$ V, and an ideality factor of $n = 1.82 \pm 0.12$ for the InP nanowires covered by native oxide. Furthermore, I utilized the vacuum system to remove the surface oxide accumulated on the nanowires during their transport by hydrogen treatment. The setup allows nanowire transfer to the preparation chamber without exposure to the ambient pressure. Through a resistive sample heating holder, the sample was annealed to approximately 400° C for 30 min and pressure of $1x10^{-6}$ mbar, which is created by a hydrogen cracker operated at 1700° C. Successful surface oxide removal was demonstrated on laterally deposited InP nanowires as shown previously in Fig. 4.26(b). (red curves).

Removal of the native oxide led to a decrease of the V_{OC} by 0.05 V, while re-oxidation significantly improved both V_{OC}, I_{SC}, and n. This $I-V$ behavior confirms that native oxide passivating the surface is beneficial for a higher V_{OC}, as it reduces recombination.

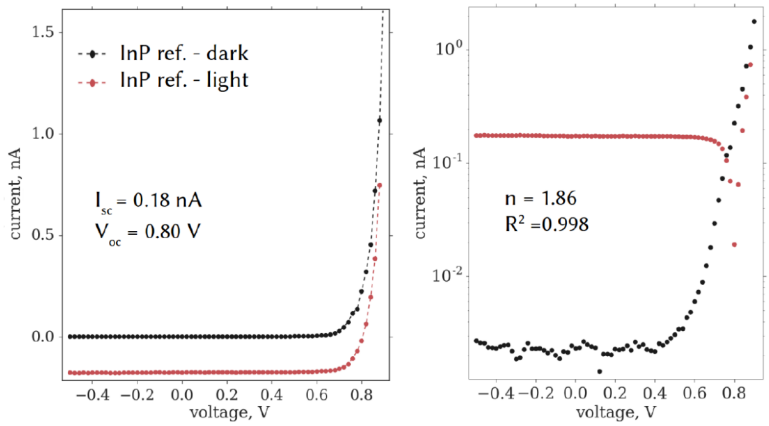

Figure 4.28: Measured *I-V* characteristics of a representative InP NW in dark (black) and light (red) conditions. Linear (left) and semi-log (right) scale show the photovoltaic parameters V_{oc} and I_{sc} as well as the ideality factor n, obtained over a voltage range of 0.65 and 0.9 V.

Chapter 5

Concluding remarks and outlook

The main goal of this thesis was to investigate nanostructures that can help solving societal challenges in energy saving and harvesting, using scanning probe techniques.

Although seemingly focused on characterization of surfaces, this is only one side of the coin. Proper understanding of nanostructures requires combined efforts of a flow of interaction between the epitaxial grower and the person investigating the resulting sample properties. With this, I should rephrase, the focus of this work to be characterization of material and crystal properties in conjunction with systematic exploration of growth conditions. This mentality has lead to Paper I and II where a combination of complementary SPM studies, in close interaction with growth experts who interpreted the influence of specific growth conditions and improved them iteratively, resulted in an in-depth understanding of the origin and formation of defects and domains in planar GaN, developed in a novel fashion which potentially can lead to improved substrates for power electronics. Going forward, a study of the local strain, tilt, and defect distribution using the synchrotron-based x-ray imaging and diffraction thereby correlating strain with a specific type of defect, will be promising next steps.

We have shown that LED nanoplatelets can be realized when keeping the epitaxial layers needed for LED functionality sufficiently thin (Paper III), although dislocations were still formed due to the large In content between layers. In Paper IV significant improvements were present, where In content of 17 % is achieved and resulted platelets are dislocation-free. This approach is believed to offer realization of four monochromatic light sources, namely red-green-blue-yellow, which then could be used in direct-view display technology. Furthermore, it offers the opportunity to make higher efficiency devices by fabricating QDs (paper V) as additional approach, for realizing longer wavelengths. AFM contributed to all these approaches by revealing the *c*-plane nucleation sites, defects, and surface morphology.

An interesting future experiment would entail measuring the wavelength of a single platelet LED contacted with the c-AFM tip through a whole range of tip-loading forces. This will result in a study of how piezoelectric and semiconductor properties as a function of tip induced local strain influence the optical behavior of LED platelets. Furthermore, by combining the AFM setup with x-ray nanofocus diffraction technique, characterization of Joule heating, piezoelectric response, and polarization induced by the AFM probe during device performance will be possible. Finally, and along the same direction, x-ray diffraction could provide information on degradation of devices through defect enhancement during the single platelet LED performance.

Characterization of novel nanostructure devices through full fabrication including all process steps will allow complete understanding of the science behind. Combination of complementary surface characterization techniques can lead to in-depth understanding of device properties, as shown for InP NW pn-junctions (Paper VI). A novel, clean, fast, and more direct method has been devised (in Paper VII) in which the STM tip serves as a nanoelectrode aiding towards investigation of photovoltaic properties of individual as-grown nanowires. This method offers a great capability of exploring the surfaces in ultrahigh vacuum environment where surface modification techniques are readily available. It provides a direct way of characterizing device behavior stemming from the impact of processing steps such as deposition of dielectric coatings, metal contacts, etc. The next step forward is to develop a better recipe for hydrogen cleaning parameters, characterize passivated and as-grown nanowires, and finally, study the photovoltaic behavior of complex multi-junction solar cells.

Although nanostructures provide clear novel opportunities, it is not straight-forward to see which of them in the end can provide the solutions needed in our increasing demand for energy on a sustainable basis. It is the responsibility of thorough characterization to show which directions are problematic and which are promising for further optimization and future devices, for which a detailed understanding of the correlations of structure, surface, and functionality at the nanoscale is crucial.

References

[1] Agora energiewende and sandbag (2019): The european power sector in 2018. up-to-date analysis on the electricity transition. https://sandbag.org.uk/wp-content/uploads/2019/01/The-European-Power-Sector-in-2018-1.pdf. Accessed: 2019-09-23.

[2] Led lighting. https://www.energy.gov/energysaver/save-electricity-and-fuel/lighting-choices-save-you-money/led-lighting. Accessed: 2019-09-09.

[3] Zhiyong Fan, Daniel J Ruebusch, Asghar A Rathore, Rehan Kapadia, Onur Ergen, Paul W Leu, and Ali Javey. Challenges and prospects of nanopillar-based solar cells. *Nano Research*, 2(11):829, 2009.

[4] Wengang Wayne Bi, Haochung Henry Kuo, Peicheng Ku, and Bo Shen. *Handbook of GaN Semiconductor Materials and Devices*. CRC Press, 2017.

[5] Yuh-Renn Wu, C-Y Huang, Yuji Zhao, and James Speck. Nonpolar and semipolar leds. In *Nitride Semiconductor Light-Emitting Diodes (LEDs)*, pages 273–295. Elsevier, 2018.

[6] Daisuke Ueda. Properties and advantages of gallium nitride. In *Power GaN Devices*, pages 1–26. Springer, 2017.

[7] JL Lyons, A Janotti, and CG Van de Walle. Effects of carbon on the electrical and optical properties of inn, gan, and aln. *Physical Review B*, 89(3):035204, 2014.

[8] Derek Hull and David J Bacon. *Introduction to dislocations*, volume 37. Elsevier, 2011.

[9] Michael A Reshchikov and Hadis Morkoç. Luminescence properties of defects in gan. *Journal of applied physics*, 97(6):5–19, 2005.

[10] Tosja K Zywietz, Jörg Neugebauer, and Matthias Scheffler. The adsorption of oxygen at gan surfaces. *Applied physics letters*, 74(12):1695–1697, 1999.

[11] VM Bermudez. Study of oxygen chemisorption on the gan (0001)-(1× 1) surface. *Journal of applied physics*, 80(2):1190–1200, 1996.

[12] K Prabhakaran, TG Andersson, and K Nozawa. Nature of native oxide on gan surface and its reaction with al. *Applied Physics Letters*, 69(21):3212–3214, 1996.

[13] SD Wolter, BP Luther, DL Waltemyer, C Önneby, Suzanne E Mohney, and RJ Molnar. X-ray photoelectron spectroscopy and x-ray diffraction study of the thermal oxide on gallium nitride. *Applied Physics Letters*, 70(16):2156–2158, 1997.

[14] C Wetzel, T Suski, JW Ager Iii, ER Weber, EE Haller, S Fischer, B Kt Meyer, RJ Molnar, and P Perlin. Pressure induced deep gap state of oxygen in gan. *Physical review letters*, 78(20):3923, 1997.

[15] N Koide, H Kato, M Sassa, S Yamasaki, K Manabe, M Hashimoto, H Amano, K Hiramatsu, and I Akasaki. Doping of gan with si and properties of blue m/i/n/n+ gan led with si-doped n+-layer by movpe. *Journal of Crystal Growth*, 115(1-4):639–642, 1991.

[16] JL Lyons, A Janotti, and CG Van de Walle. Carbon impurities and the yellow luminescence in gan. *Applied Physics Letters*, 97(15):152108, 2010.

[17] Unhi Honda, Yujiro Yamada, Yutaka Tokuda, and Kenji Shiojima. Deep levels in n-gan doped with carbon studied by deep level and minority carrier transient spectroscopies. *Japanese Journal of Applied Physics*, 51(4S):04DF04, 2012.

[18] Takeshi Tanaka, Naoki Kaneda, Tomoyoshi Mishima, Yuhei Kihara, Toshichika Aoki, and Kenji Shiojima. Roles of lightly doped carbon in the drift layers of vertical n-gan schottky diode structures on freestanding gan substrates. *Japanese Journal of Applied Physics*, 54(4):041002, 2015.

[19] CH Seager, AF Wright, J Yu, and W Götz. Role of carbon in gan. *Journal of applied physics*, 92(11):6553–6560, 2002.

[20] Toshio Ogino and Masaharu Aoki. Mechanism of yellow luminescence in gan. *Japanese Journal of Applied Physics*, 19(12):2395, 1980.

[21] Akira Sakai, Haruo Sunakawa, and Akira Usui. Defect structure in selectively grown gan films with low threading dislocation density. *Applied Physics Letters*, 71(16):2259–2261, 1997.

[22] J. Elsner, R. Jones, P. K. Sitch, V. D. Porezag, M. Elstner, Th. Frauenheim, M. I. Heggie, S. Öberg, and P. R. Briddon. Theory of threading edge and screw dislocations in gan. *Phys. Rev. Lett.*, 79:3672–3675, Nov 1997.

[23] D Kapolnek, XH Wu, B Heying, S Keller, BP Keller, UK Mishra, SP DenBaars, and JS Speck. Structural evolution in epitaxial metalorganic chemical vapor deposition grown gan films on sapphire. *Applied Physics Letters*, 67(11):1541–1543, 1995.

[24] Dongsheng Li, M Sumiya, S Fuke, Deren Yang, Duanlin Que, Y Suzuki, and Y Fukuda. Selective etching of gan polar surface in potassium hydroxide solution studied by x-ray photoelectron spectroscopy. *Journal of Applied Physics*, 90(8):4219–4223, 2001.

[25] Wataru Utsumi, Hiroyuki Saitoh, Hiroshi Kaneko, Tetsu Watanuki, Katsutoshi Aoki, and Osamu Shimomura. Congruent melting of gallium nitride at 6 gpa and its application to single-crystal growth. *Nature materials*, 2(11):735, 2003.

[26] Dirk Ehrentraut, Elke Meissner, and Michal Bockowski. *Technology of gallium nitride crystal growth*, volume 133. Springer Science & Business Media, 2010.

[27] Gerald B Stringfellow. *Organometallic vapor-phase epitaxy: theory and practice*. Elsevier, 1999.

[28] RS Wagner and WC Ellis. Vapor-liquid-solid mechanism of single crystal growth. *Applied physics letters*, 4(5):89–90, 1964.

[29] BJ Ohlsson, Mikael T Björk, MH Magnusson, K Deppert, Lars Samuelson, and LR Wallenberg. Size-, shape-, and position-controlled gaas nano-whiskers. *Applied Physics Letters*, 79(20):3335–3337, 2001.

[30] MT Björk, BJ Ohlsson, T Sass, AI Persson, Claes Thelander, MH Magnusson, Knut Deppert, LR Wallenberg, and Lars Samuelson. One-dimensional steeplechase for electrons realized. *Nano Letters*, 2(2):87–89, 2002.

[31] Gaute Otnes. *III-V nanowire solar cells: Growth and characterization*. Lund University, 2018.

[32] Harvey T Dobbs, Dimitri D Vvedensky, Andrew Zangwill, Jonas Johansson, Niclas Carlsson, and Werner Seifert. Mean-field theory of quantum dot formation. *Physical review letters*, 79(5):897, 1997.

[33] BO Monemar, PP Paskov, Galia Pozina, Carl Hemmingsson, JP Bergman, T Kawashima, H Amano, I Akasaki, T Paskova, S Figge, et al. Evidence for two mg related acceptors in gan. *Physical review letters*, 102(23):235501, 2009.

[34] Bo Monemar, PP Paskov, Galia Pozina, Carl Hemmingsson, JP Bergman, H Amano, I Akasaki, S Figge, D Hommel, Tanja Paskova, et al. Mg-related acceptors in gan. *physica status solidi c*, 7(7-8):1850–1852, 2010.

[35] Bo Monemar, PP Paskov, Galia Pozina, Carl Hemmingsson, JP Bergman, Sergey Khromov, VN Izyumskaya, V Avrutin, X Li, H Morkoç, et al. Properties of the main mg-related acceptors in gan from optical and structural studies. *Journal of Applied Physics*, 115(5):053507, 2014.

[36] Frank Glas. Critical dimensions for the plastic relaxation of strained axial heterostructures in free-standing nanowires. *Physical Review B*, 74(12):121302, 2006.

[37] Nicklas Anttu and H. Q. Xu. Efficient light management in vertical nanowire arrays for photovoltaics. *Opt. Express*, 21(S3):A558–A575, May 2013.

[38] Nicklas Anttu and HQ Xu. Efficient light management in vertical nanowire arrays for photovoltaics. *Optics express*, 21(103):A558–A575, 2013.

[39] Muyi Chen, Eiji Nakai, Katsuhiro Tomioka, and Takashi Fukui. Application of free-standing inp nanowire arrays and their optical properties for resource-saving solar cells. *Applied Physics Express*, 8(1):012301, 2014.

[40] Hannah J Joyce, Jennifer Wong-Leung, Chaw-Keong Yong, Callum J Docherty, Suriati Paiman, Qiang Gao, H Hoe Tan, Chennupati Jagadish, James Lloyd-Hughes, Laura M Herz, et al. Ultralow surface recombination velocity in inp nanowires probed by terahertz spectroscopy. *Nano letters*, 12(10):5325–5330, 2012.

[41] Magnus T Borgström, Jesper Wallentin, Johanna Trägårdh, Peter Ramvall, Martin Ek, L Reine Wallenberg, Lars Samuelson, and Knut Deppert. In situ etching for total control over axial and radial nanowire growth. *Nano Research*, 3(4):264–270, 2010.

[42] Gaute Otnes, Enrique Barrigón, Christian Sundvall, K Erik Svensson, Magnus Heurlin, Gerald Siefer, Lars Samuelson, Ingvar Åberg, and Magnus T Borgström. Understanding inp nanowire array solar cell performance by nanoprobe-enabled single nanowire measurements. *Nano letters*, 18(5):3038–3046, 2018.

[43] Dick van Dam, Niels JJ van Hoof, Yingchao Cui, Peter J van Veldhoven, Erik PAM Bakkers, Jaime Gómez Rivas, and Jos EM Haverkort. High-efficiency nanowire solar cells with omnidirectionally enhanced absorption due to self-aligned indium–tin–oxide mie scatterers. *ACS nano*, 10(12):11414–11419, 2016.

[44] Nicklas Anttu. Shockley–queisser detailed balance efficiency limit for nanowire solar cells. *Acs Photonics*, 2(3):446–453, 2015.

[45] Nicklas Anttu. Physics and design for 20% and 25% efficiency nanowire array solar cells. *Nanotechnology*, 30(7):074002, 2018.

[46] Suk Choi, Hee Jin Kim, Seong-Soo Kim, Jianping Liu, Jeomoh Kim, Jae-Hyun Ryou, Russell D Dupuis, Alec M Fischer, and Fernando A Ponce. Improvement of peak quantum efficiency and efficiency droop in iii-nitride visible light-emitting diodes with an inaln electron-blocking layer. *Applied Physics Letters*, 96(22):221105, 2010.

[47] Tae-Yeon Seong, Jung Han, Hiroshi Amano, and Hadis Morkoç. *III-Nitride based light emitting diodes and applications*. Springer, 2013.

[48] Govind P Agrawal and Niloy K Dutta. *Semiconductor lasers*. Springer Science & Business Media, 2013.

[49] Vincenzo Fiorentini, Fabio Bernardini, Fabio Della Sala, Aldo Di Carlo, and Paolo Lugli. Effects of macroscopic polarization in iii-v nitride multiple quantum wells. *Physical Review B*, 60(12):8849, 1999.

[50] Thi Huong Ngo, Bernard Gil, Benjamin Damilano, Kaddour Lekhal, and Philippe De Mierry. Internal quantum efficiency and auger recombination in green, yellow and red ingan-based light emitters grown along the polar direction. *Superlattices and Microstructures*, 103:245–251, 2017.

[51] Houqiang Fu, Zhijian Lu, and Yuji Zhao. Analysis of low efficiency droop of semipolar ingan quantum well light-emitting diodes by modified rate equation with weak phase-space filling effect. *AIP Advances*, 6(6):065013, 2016.

[52] K Hiramatsu, Y Kawaguchi, M Shimizu, N Sawaki, T Zheleva, Robert F Davis, H Tsuda, W Taki, N Kuwano, and K Oki. The composition pulling effect in movpe grown ingan on gan and algan and its tem characterization. *Materials Research Society Internet Journal of Nitride Semiconductor Research*, 2, 1997.

[53] Gerd Binnig, Calvin F Quate, and Ch Gerber. Atomic force microscope. *Physical review letters*, 56(9):930, 1986.

[54] Gerd Binnig and Heinrich Rohrer. Scanning tunneling microscopy. *Surface science*, 126(1-3):236–244, 1983.

[55] M Nonnenmacher, MP o'Boyle, and H Kumar Wickramasinghe. Kelvin probe force microscopy. *Applied physics letters*, 58(25):2921–2923, 1991.

[56] JR Matey and J Blanc. Scanning capacitance microscopy. *Journal of Applied Physics*, 57(5):1437–1444, 1985.

[57] Atomic force microscopy. `http://www.nanoscience.de/HTML/methods/afm.html`. Accessed: 2019-09-09.

[58] Nanoandmore. https://www.nanoandmore.com/. Accessed: 2019-09-09.

[59] Ricardo García. *Amplitude modulation atomic force microscopy*. John Wiley & Sons, 2011.

[60] Dimension icon user quide.

[61] G Binnig, Ch Gerber, E_ Stoll, TR Albrecht, and CF Quate. Atomic resolution with atomic force microscope. *EPL (Europhysics Letters)*, 3(12):1281, 1987.

[62] Chanmin Su, Jian Shi, Yan Hu, Shuiqing Hu, and Ji Ma. Method and apparatus of using peak force tapping mode to measure physical properties of a sample, March 22 2016. US Patent 9,291,640.

[63] TR Albrecht, Pr Grütter, D Horne, and D Rugar. Frequency modulation detection using high-q cantilevers for enhanced force microscope sensitivity. *Journal of Applied Physics*, 69(2):668–673, 1991.

[64] Yves Martin, Clayton C Williams, and H Kumar Wickramasinghe. Atomic force microscope–force mapping and profiling on a sub 100-å scale. *Journal of Applied physics*, 61(10):4723–4729, 1987.

[65] Jian Shi, Yan Hu, Shuiqing Hu, Ji Ma, and Chanmin Su. Method and apparatus of using peak force tapping mode to measure physical properties of a sample, February 11 2014. US Patent 8,650,660.

[66] Bede Pittenger, Natalia Erina, and Chanmin Su. Mechanical property mapping at the nanoscale using peakforce qnm scanning probe technique. In *Nanomechanical analysis of high performance materials*, pages 31–51. Springer, 2014.

[67] Daniel Maugis. *Contact, adhesion and rupture of elastic solids*, volume 130. Springer Science & Business Media, 2013.

[68] Thomas Stifter, Othmar Marti, and Bharat Bhushan. Theoretical investigation of the distance dependence of capillary and van der waals forces in scanning force microscopy. *Physical Review B*, 62(20):13667, 2000.

[69] John E Sader, Ian Larson, Paul Mulvaney, and Lee R White. Method for the calibration of atomic force microscope cantilevers. *Review of Scientific Instruments*, 66(7):3789–3798, 1995.

[70] John E Sader, James WM Chon, and Paul Mulvaney. Calibration of rectangular atomic force microscope cantilevers. *Review of scientific instruments*, 70(10):3967–3969, 1999.

[71] John E Sader, Jessica Pacifico, Christopher P Green, and Paul Mulvaney. General scaling law for stiffness measurement of small bodies with applications to the atomic force microscope. *Journal of Applied physics*, 97(12):124903, 2005.

[72] Jeffrey L Hutter and John Bechhoefer. Calibration of atomic-force microscope tips. *Review of Scientific Instruments*, 64(7):1868–1873, 1993.

[73] H-J Butt and Manfred Jaschke. Calculation of thermal noise in atomic force microscopy. *Nanotechnology*, 6(1):1, 1995.

[74] Carlos Bustamante and David Keller. Scanning force microscopy in biology. *Physics Today*, 48:32, 1995.

[75] Nevill Francis Mott and Harry Jones. *The theory of the properties of metals and alloys*. Courier Corporation, 1958.

[76] John Bardeen. Surface states and rectification at a metal semi-conductor contact. *Physical Review*, 71(10):717, 1947.

[77] Abraham Many, Yehuda Goldstein, and Norman B Grover. Semiconductor surfaces. 1965.

[78] Emlyn Huw Rhoderick. Metal-semiconductor contacts. *IEE Proceedings I-Solid-State and Electron Devices*, 129(1):1, 1982.

[79] Yu K Ryu and Ricardo Garcia. Advanced oxidation scanning probe lithography. *Nanotechnology*, 28(14):142003, 2017.

[80] John A Dagata, J Schneir, Howard H Harary, CJ Evans, Michael T Postek, and J Bennett. Modification of hydrogen-passivated silicon by a scanning tunneling microscope operating in air. *Applied Physics Letters*, 56(20):2001–2003, 1990.

[81] Urszula Gasser, Martin Sigrist, Simon Gustavsson, Klaus Ensslin, and Thomas Ihn. Double layer local anodic oxidation using atomic force microscopy. In *Tip-Based Nanofabrication*, pages 91–127. Springer, 2011.

[82] M Sigrist, A Fuhrer, T Ihn, K Ensslin, DC Driscoll, and AC Gossard. Multiple layer local oxidation for fabricating semiconductor nanostructures. *Applied physics letters*, 85(16):3558–3560, 2004.

[83] Ramses V Martínez, Javier Martínez, and Ricardo Garcia. Silicon nanowire circuits fabricated by afm oxidation nanolithography. *Nanotechnology*, 21(24):245301, 2010.

[84] Farhad Larki, Arash Dehzangi, Alam Abedini, Ahmad Makarimi Abdullah, Elias Saion, Sabar D Hutagalung, Mohd N Hamidon, and Jumiah Hassan. Pinch-off mechanism in double-lateral-gate junctionless transistors fabricated by scanning probe microscope based lithography. *Beilstein journal of nanotechnology*, 3(1):817–823, 2012.

[85] Javier Martinez, Ramses Valentin Martinez, and Ricardo Garcia. Silicon nanowire transistors with a channel width of 4 nm fabricated by atomic force microscope nanolithography. *Nano letters*, 8(11):3636–3639, 2008.

[86] Niandong Jiao, Yuechao Wang, Ning Xi, and ZaiLi Dong. Afm based anodic oxidation and its application to oxidative cutting and welding of cnt. *Science in China Series E: Technological Sciences*, 52(11):3149, 2009.

[87] S Kalinin and Alexei Gruverman Scanning Probe Micropscopy. Electrical and electromechanical phenomena at the nanoscale, volume ii, 2007.

[88] Jesper Wallentin, Nicklas Anttu, Damir Asoli, Maria Huffman, Ingvar Åberg, Martin H Magnusson, Gerald Siefer, Peter Fuss-Kailuweit, Frank Dimroth, Bernd Witzigmann, et al. Inp nanowire array solar cells achieving 13.8% efficiency by exceeding the ray optics limit. *Science*, 339(6123):1057–1060, 2013.

[89] Scm principles of operation. `http://www.nanophys.kth.se/nanophys/facilities/nfl/afm/icon/bruker-help/Content/AppModules/Operation/SCM/SCMTheory.htm`. Accessed: 2019-09-27.

[90] CC Williams. Two-dimensional dopant profiling by scanning capacitance microscopy. *Annual review of materials science*, 29(1):471–504, 1999.

[91] Hans Lüth. *Surfaces and interfaces of solid materials*. Springer Science & Business Media, 2013.

[92] Gerd Binnig, Heinrich Rohrer, Ch Gerber, and Edmund Weibel. Surface studies by scanning tunneling microscopy. *Physical review letters*, 49(1):57, 1982.

[93] Martin Hjort, Johan V Knutsson, Bernhard Mandl, Knut Deppert, Edvin Lundgren, Rainer Timm, and Anders Mikkelsen. Surface morphology of au-free grown nanowires after native oxide removal. *Nanoscale*, 7(22):9998–10004, 2015.

[94] Martin Hjort, Jesper Wallentin, Rainer Timm, Alexei A Zakharov, Ulf Hakanson, Jesper N Andersen, Edvin Lundgren, Lars Samuelson, Magnus T Borgstrom, and Anders Mikkelsen. Surface chemistry, structure, and electronic properties from microns to the atomic scale of axially doped semiconductor nanowires. *ACS nano*, 6(11):9679–9689, 2012.

[95] Rainer Timm, Olof Persson, David LJ Engberg, Alexander Fian, James L Webb, Jesper Wallentin, Andreas Jönsson, Magnus T Borgström, Lars Samuelson, and Anders Mikkelsen. Current–voltage characterization of individual as-grown nanowires using a scanning tunneling microscope. *Nano letters*, 13(11):5182–5189, 2013.